THE ASTRONOMICAL JOURNAL VOLUME 106, NUMBER 6 DECEMBER 1993

AN OCCULTATION BY SATURN'S RINGS ON 1991 OCTOBER 2–3 OBSERVED WITH *THE HUBBLE SPACE TELESCOPE*[1]

J. L. ELLIOT
Department of Earth, Atmospheric, and Planetary Sciences,[2] Massachusetts Institute of Technology, Cambridge, Massachusetts 02139-4307 and Lowell Observatory, Flagstaff, Arizona 86001
Electronic mail: jim@astron.mit.edu

A. S. BOSH AND M. L. COOKE
Department of Earth, Atmospheric, and Planetary Sciences, Massachusetts Institute of Technology, Cambridge, Massachusetts 02139-4307
Electronic mail: amanda@lowell.edu, maren@mit.edu

R. C. BLESS,[3] M. J. NELSON, J. W. PERCIVAL, AND M. J. TAYLOR
Space Astronomy Laboratory, University of Wisconsin, Madison, Wisconsin 53706
Electronic mail: bless@larry.sal.wisc.edu, nelson@larry.sal.wisc.edu, jwp@larry.sal.wisc.edu, taylor@larry.sal.wisc.edu

J. F. DOLAN
Laboratory for Astronomy and Solar Physics, Goddard Space Flight Center, Greenbelt, Maryland 20771-6810
Electronic mail: tejfd@larry.sal.wisc.edu

E. L. ROBINSON
Department of Astronomy, University of Texas, Austin, Texas 78712-1083
Electronic mail: elr.aries.as.utexas.edu

G. W. VAN CITTERS
Division of Astronomical Sciences, National Science Foundation, Washington, DC 20550
and Department of Aerospace Engineering U. S. Naval Academy, Annapolis, Maryland 21402
Electronic mail: gvancitt@note1.nsf.gov

Received 1993 May 19

ABSTRACT

An occultation of the star GSC 6323-01396 ($V=11.9$) by Saturn's rings was observed with the High-Speed Photometer on the *Hubble Space Telescope* (*HST*) on 1991 October 2–3. This occultation occurred when Saturn was near a stationary point, so the apparent motion of Saturn relative to the star was dominated by the *HST* orbital motion (8 km s^{-1}). Data were recorded simultaneously at effective wavelengths of 3200 and 7500 Å, with an integration time of 0.15 s. Observations were interrupted by passages of the spacecraft behind the Earth and through the South Atlantic Anomaly. Fifteen segments of occultation data, totaling 6.8 h, were recorded in 13 successive orbits during the 20.0 h interval from UTC 1991 October 2, 19:35 until UTC 1991 October 3, 15:35. Occultations by 43 different features throughout the classical rings were unambiguously identified in the light curve, with a second occultation by 24 of them occurring due to spacecraft orbital parallax during this extremely slow event. Occultation times for features currently presumed circular were measured and employed in a geometrical model for the rings. This model, relating the observed occultation times to feature radii and longitudes, is presented here and is used in a least-squares fit for the pole direction and radius scale of Saturn's ring system. Combined fits with the *HST* occultation times and 28 Sgr occultation times [French *et al.*, Icarus, 103, 163 (1993) and Hubbard *et al.*, Icarus, 103, 215 (1993)] yield a ring-pole direction of $\alpha=40^{\circ}.5929\pm0^{\circ}.0151$ and $\delta=83^{\circ}.5348\pm0^{\circ}.0053$ (J2000.0, at the Voyager 1 epoch of UTC 1980 Nov. 12 23:46:32). This result, independent of Voyager data and its associated trajectory errors, is compared with other recent determinations of the pole and radius scale.

1. INTRODUCTION

Saturn's rings exhibit a wide variety of dynamical phenomena. From Earth-based observations prior to spacecraft flybys the overall structure of the A, B, and C rings had been identified, and the Cassini division separating the A and B rings had been associated with the 2:1 resonance with Mimas (Alexander 1962; Elliot & Kerr 1984). Also, a narrow division in the A ring (now called the Encke gap) had been observed as early as 1888 (Keeler 1889). As a result of the dramatic increase in spatial resolution available to the flyby spacecraft Voyagers 1 and 2, many new phenomena were discovered in Saturn's rings: gaps, moonlets, wakes, spiral density waves, bending waves, and narrow ringlets (Cuzzi *et al.* 1984). In addition to their in-

[1]Based on observations with the NASA/ESA *Hubble Space Telescope*, obtained at the Space Telescope Science Institute, which is operated by the Association of Universities for Research in Astronomy, Inc., under NASA Contract No. NAS5-26555.
[2]Also Department of Physics.
[3]Also Department of Astronomy.

 0004-6256/93/106(6)/2544/29/$0.90

trinsic interest, precise modeling of these phenomena—especially their dynamical relationships and their interactions with Saturn's inner satellites—teaches us about fundamental processes that occur in particle disks. Furthermore, better understanding of these processes and how they affect ring evolution will be needed before we can reliably infer the age of Saturn's rings. The evidence now points to the conclusion that at least the A ring is young (Esposito 1986).

Further kinematic and dynamical studies of Saturn's rings require that we continually probe them with high spatial resolution. The only Earth-based method that allows us to achieve kilometer-scale spatial resolution is the stellar occultation technique (Elliot 1990). A notable achievement of this technique has been the development of a kinematic model for the Uranian rings over the decade between their discovery and the Voyager encounter in 1986 (Elliot *et al.* 1978; French *et al.* 1988). This development included the first examples of narrow rings (Elliot *et al.* 1977), eccentric rings (Nicholson *et al.* 1978), and inclined rings (French *et al.* 1982). Because the zones of occultation visibility on Earth are limited, mobile Earth-based observational platforms and fixed telescopes have been used to advantage for this work: for example, the Kuiper Airborne Observatory (Elliot *et al.* 1977; Dunham *et al.* 1982) and small, portable telescopes (Baron *et al.* 1983).

The goals of stellar occultation observers have been to learn more from new data sets by (i) acquiring occultation light curves with higher signal-to-noise ratio and greater spatial resolution, (ii) achieving greater spatial coverage by including more observing stations per event, (iii) obtaining light curves over a greater range of wavelengths, and (iv) increasing the time coverage of kinematic phenomena by observing more events. Toward these goals, the promise of the High Speed Photometer (HSP; Bless *et al.* 1993) on the *Hubble Space Telescope* (*HST*) was several-fold: there would be access to ultraviolet wavelengths, no clouds, no scintillation noise, and small focal-plane apertures that would admit lower levels of background light (and associated noise) into the occultation light curves.

The spherical aberration of the *HST* optics, however, has diminished the effectiveness of the *HST* for occultation observations in several ways: (i) due to the large point spread function (PSF; see Fig. 2 in Burrows *et al.* 1991), the signal level from a star within the focal plane aperture has been reduced by about 50%, (ii) the background level on the wings of the PSF from nearby bright objects (e.g., the occulting planets) has increased, and (iii) modulation of the large PSF by pointing jitter adds more noise to the data than had been anticipated. An additional diminution of occultation capability of the *HST* is that NASA's selected fix for the aberration problem—the installation of COSTAR—will require the removal of the HSP altogether near the end of 1993.

In spite of these difficulties, the *HST* now provides unique opportunities for occultation work, and in this paper we present the HSP observations of the occultation of the star GSC 6323-01396 by Saturn's rings that occurred in 1991 October (Bosh & McDonald 1992). A notable feature of this occultation is that it occurred near one end of Saturn's retrograde loop, so that the geocentric shadow velocity was 1–2 km s^{-1}, and ring egress lasted for 20 h. Since the orbital velocity of the *HST* is about 8 km s^{-1} and the orbit greater than one Earth diameter across, several regions of the rings were probed twice in spite of the unavoidable shutdown of data recording during Earth occultation and passages through the South Atlantic Anomaly (SAA). Hence this data set has some of the advantages of multiple station observations of a single event, such as the 28 Sgr occultation by Saturn that occurred in 1989 July (French *et al.* 1993; Hubbard *et al.* 1993; Harrington *et al.* 1993). These references will be referred to henceforth as F93, Hu93, and Ha93.

In this paper we present the light curves of the occultation, from which we measure occultation times for previously identified, circular features. These times are then used—in combination with the 28 Sgr data given in F93 and Hu93–in a least-squares solution for the radius scale and position of the ring-plane pole of Saturn.

2. PREPARATION FOR OBSERVATIONS

Preparation for occultation observations with the *HST* occurs in four stages: (i) selecting an event that will have sufficient signal to noise and observability to achieve the desired objectives; (ii) planning the sequence of exposures needed to acquire the occultation light curve and calibration data; (iii) updating the spacecraft observing plan ("proposal") as necessary (with improved star coordinates, etc.); and (iv) checking the derived spacecraft commands in order to increase the chances that the desired data will be recorded.

2.1 Occultation Signal to Noise and Observability

The occultation of GSC 6323-01396 was identified from a search of the *HST Guide Star Catalog* for Saturn occultation candidates by Bosh & McDonald (1992), and the colors of this star were measured by Sybert *et al.* (1992): $V=11.9$, $B-V=0.7$, $V-R=0.5$. For stars that do not have large UV fluxes (such as this one), our preferred mode of observation is the 'SPLIT" mode of the HSP, which provides simultaneous data recording at 3200 and 7500 Å (Bless *et al.* 1992, also Table 1). In the presence of background light from the brightest parts of Saturn's rings, a total occultation of the star would be about 1% of the background, according to "HSPSIM," a program that calculates the expected throughput for any channel of the HSP from the magnitude and spectral type of the star (Percival 1993). Considering only photon noise from this background ring light, a total occultation of the star lasting 1.0 s would have a signal-to-noise ratio of 17 for the 7500 Å channel. This would be adequate to record most of the sharp-edged features in Saturn's rings with a spatial resolution of about a kilometer.

Another source of noise that must be considered for HSP occultation photometry is the modulation of the background and stellar signal due to jitter of the telescope

TABLE 1. HSP instrumental parameters relevant to occultations.

Parameter	"VIS" Channel	"PMT" Channel
Detector Type	image dissector	photomultiplier
Photocathode Type	bialkali	GaAs
Dark (s^{-1})	0.2	349
Signal for 1% Nonlinearity (s^{-1})	2.5×10^5	2.5×10^5
Central Wavelength (Å)	3200	7500
Bandpass (FWHM, Å)	100	1600
Aperture Diameter (arcsec)	1.0	1.0
Sky (s^{-1})	0.015	2.6
Source[a] for V=11.9[b] (s^{-1})	410	7000
Ring background at outer edge of A Ring (s^{-1})	2.7×10^4	3.7×10^5
Ring background in central B Ring (s^{-1})	5.0×10^4	1.3×10^6
S/N[c] at outer edge of A Ring	2.6	11.2
S/N[c] in the central B Ring	1.8	6.3

Notes to TABLE 1

[a]For the 60% of the total light admitted by the 1-arcsec aperture

[b]B–V=0.7, V–R=0.5

[c]Ratio of unocculted star signal to background noise for an integration time of 1.0 s calculated from rms variation of the background.

in "coarse track" guidance mode. An example of this from a Science Verification (SV) test for Saturn ring occultations (SV2771) is shown in Fig. 1, where the modulations have a peak amplitude equivalent to the flux from a star with $R=11.5$ and a period of 10–15 s (the period of the coarse track mechanism). These modulations are particularly severe when observing in a bright and varying background, but can be avoided if guide stars brighter than magnitude 13.0 are available and the "fine lock" tracking mode used. It has been our experience for occultation work that guide stars suitable for fine lock are available within the allowed ±30° roll for the spacecraft about 20% of the time. Fortunately, fine lock could be used for the observations of GSC 6323-01396.

A second consideration for selecting an occultation is

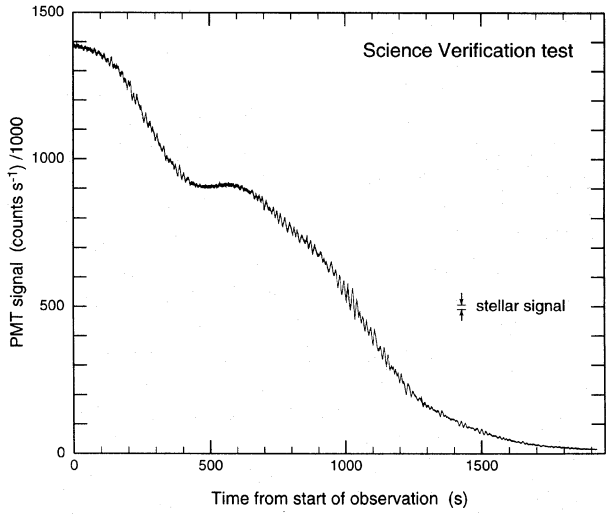

FIG. 1. SV 2771 light curve, illustrating the disastrous effects of jitter while in coarse track. The approximate stellar contribution to the total signal is indicated (for $V=13.0$, $B-V=0.8$; Sybert *et al.* 1992), and is only about half the maximum jitter amplitude.

the observability of the event with the *HST*. Generous avoidance zones for the Sun (50°), anti-Sun (7°), and Moon (14°) allow only about 63% of stellar occultations by solar system bodies to be safely observed. Also, because the *HST* is in a low-Earth orbit—in contrast with *IUE* (Boggess *et al.* 1978a; Boggess *et al.* 1978b)—the Earth causes significant interference. Specifically, an occultation is not observable due to limits imposed by the Earth if it occurs (i) during Earth occultation for the *HST*, (ii) within 10° of the bright Earth limb or within 5° of the dark limb, (iii) during *HST* passage over the SAA, or (iv) during the 5 minutes needed for reacquisition of the target by the *HST* after emerging from the Earth-limb avoidance limits. For short occultations (lasting a small fraction of an *HST* orbit), these factors reduce the fraction of observable events by another 67%—leaving only 21% of potential short occultations observable by the *HST*. For long occultations that are not prohibited because they are too close to the Sun or Moon—such as the present one—the avoidance factors associated with the Earth allow only about 33% of the data to be recorded. The exact value of this factor depends on the orientation of the *HST* orbit pole within its 2 month precession cycle and the declination of the object being observed.

Due to uncertainties in predicting the atmospheric drag on the *HST*, its orbital longitude cannot be known with certainty many months in advance. Hence in the early stages of planning occultation observations, one can know only the length of the data-recording window for an orbit. If this would be inadequate (no matter what the orbital phase of the *HST* might turn out to be) then the occultation can be rejected. More commonly the case, however, is that one must wait until about 60 days prior to the event (when the predicted orbital longitude has an error of about 25°) to learn enough about the time intervals when data can be recorded in order to decide whether observations should be attempted.

GSC 6323-01396 was occulted twice near one extremum

of Saturn's retrograde loop. Each occultation lasted many hours, so that complete coverage of both occultations would have used almost all of our time available for occultation work. We decided that this would be too great a risk, because the execution of these observations occurred only 27 days after the SV test for occultations—an interval too short to allow changes of spacecraft commands for this observation in response to lessons learned from the SV test. Therefore we limited our observations to the first egress event (1991 October 2–3), since it would have the greatest radial resolution of the four events. We would acquire the star soon after planet egress, when it would be behind the D ring, and follow it past F ring egress.

2.2 Planning the Observations

For *HST* observations of stellar occultations, the planning stage is crucial because spacecraft instructions have to be finalized well in advance of the event. Although real-time control of observations is an option, this is impractical for stellar occultations because of the heavy constraints it places on the observing windows. In order to perform observations in real-time, a contact with the Tracking and Data Relay Satellite System (TDRSS) must be available throughout the observations. This adds considerably to scheduling difficulties, since the fraction of time that TDRSS is available to *HST* is limited to an average of 20%, and the times for TDRSS contacts are determined by priorities other than the needs of the *HST*. Therefore we chose to have no real-time components in our observations in order to increase the amount of data we could collect.

As discussed earlier, the "SPLIT" mode of the HSP would be the most suitable instrumental configuration for this occultation, since it would provide the greatest throughput of starlight and allow simultaneous light curves to be obtained at 3200 and 7500 Å (Bless *et al.* 1992, 1994). The detector in the 7500 Å channel is a photomultiplier tube (PMT) employing a GaAs photocathode for large throughput of red light. The optical path to the PMT contains a dichroic beamsplitter that routes the 3200 Å light to one of the image dissector tubes (the "VIS IDT," having a bialkali photocathode) for simultaneous data recording with both detectors. This mode is useful for removal of background light from the rings when they have a different relative flux from the occulted star in the two channels (Elliot *et al.* 1975). For stars that have adequate flux in the UV, these data can also be used to probe the composition of planetary atmospheres through the "spike-delay" technique (Elliot *et al.* 1974), or to probe the particle-size distribution of ring particles by studying differential extinction (Marouf *et al.* 1983).

The HSP can collect data in both digital and analog modes ("formats"). The digital format counts pulses but must be corrected for dead-time ($\tau \sim 40$ ns) count losses at high count rates (Bless *et al.* 1992). The analog format measures flux at a variable sample interval that is always shorter than 5 ms (Bless *et al.* 1992). Since the signal is sampled rather than integrated, however, it yields a much lower signal-to-noise ratio than the digital recording format. Hence we recorded data in both formats simultaneously, using the digital signal for analysis and the analog signal to calibrate the dead-time correction, if necessary.

The occultation exposures were set to record data for as long as possible (between SAA passages and Earth occultations), and the criterion for selecting the integration time was on the basis of radial resolution. The spatial resolution of occultation data is determined by the time resolution and signal-to-noise ratio of the data, the angular diameter that the occulted star subtends at the planet, and the Fresnel scale at the planet ($\sqrt{\lambda D/2}$, where λ is the wavelength of observation and D is the distance from the observer to the occulting body). The stellar size and the Fresnel scale depend on the particular occultation event, and ideally one would set the data integration time to oversample the resolution limit set by diffraction or stellar diameter by at least a factor of two. As estimated from its magnitude and colors (Sybert *et al.* 1992), the angular diameter of the star, projected at the distance of Saturn is 0.3 km—smaller than the Fresnel scale of 0.7 km (for the 7500 Å channel). Radial shadow velocities relevant to this event lie within the range 0–8 km s^{-1}. Hence, the minimum time for crossing 0.7 km would be 0.088 s, dictating an integration time of less than 0.044 s. Although instrumental restrictions (which have since been removed) for this data format in the SPLIT mode would allow an integration time as short as 0.06 s, we chose a somewhat longer time—0.15 s—in order to be well clear of the absolute limit. Even with this integration time, the spatial resolution was limited by the signal-to-noise ratio of the data, rather than by the integration time.

For the reduction of occultation data, knowledge of the absolute timing is critical. As data are sent from the spacecraft, time tags from the spacecraft clock are attached, and later converted to UTC. The calibration is specified to be correct to within 10 ms, and observations of the Crab pulsar show this to be the case (Percival *et al.* 1993). The calibration procedure for times reported by the *HST* clock has been described by Percival (1992).

When observing occultations by Saturn's rings at visible wavelengths, the accuracy of the derived optical depths of the rings is limited by the accuracy with which one can subtract the bright planet and ring background from the light curve. Previous Earth-based observations of Saturn ring occultations have either been in the infrared, where Saturn and its rings have several deep absorption bands, making them appear quite dark; or with imaging detectors such as CCDs, so that the ring background can later be removed through modeling (see F93, Ha93, Hu93, and references therein). With the *HST*, neither approach is possible: the Wide Field/Planetary Camera is not capable of reading out fast enough for occultation observations (MacKenty *et al.* 1992). The minimum time between integrations is 2 min, which translates into over a thousand Fresnel scales for this event. The Faint Object Camera is even slower, with 4–5 min between integrations (Paresce 1992), and there are no infrared detectors currently on the *HST*. The Faint Object Spectrograph (FOS) can be used

for occultation observations, but it cannot record a continuous time series (Kinney 1993).

Our strategy for dealing with the background from the planet and rings involved mapping the background light. We performed 14 scans of Saturn and its rings, across a region that would include the apparent path of the star through the system (Fig. 2). The width of the smallest rectangle enclosing the stellar path is larger than the 1 arcsec aperture used (see Fig. 4); therefore, a single scan of the background following the middle of the path would not produce sufficient information about the background light entering the aperture during the occultation data collection. To overcome this, we planned a set of scans, offset from each other in the direction perpendicular to the apparent star path. In this manner we intended to map all parts of the rings that were included in the aperture during the occultation observations. We also collected 5 min of dark sky measurements in order to characterize the noise from the detector itself.

Finally, we consider the issue of acquiring the star near a large, bright object like Saturn. The most commonly used mode of target acquisition on the HSP is the onboard acquisition (Bless *et al.* 1992). In this mode, the 10 arcsec finding aperture is scanned on a 20×20 grid (the default setting). The center of the star is found from this raster scan, the process is repeated with the result of the first scan as the center of the second scan, and then the star is offset from the finding aperture to the 1 arcsec aperture. This mode fails in crowded fields or in fields with large background gradients. Because we were attempting to start the occultation observations while the star was behind the D Ring, we could not use the onboard acquisition method because the gradients produced by the bright ring and planet background would have been too large. Instead, we used the offset acquisition method. For this method, we perform an onboard acquisition on a nearby star, away from Saturn. We center on this star, and then perform a blind offset to the target star, GSC 6323-01396. The limitations imposed on this method are: (i) as the offset target, we must use a star close enough so that the error introduced by the blind offset under gyro control ($\sim$0.002 arcsec s^{-1}) will be small enough to keep the star well centered, (ii) the offset and target stars must be close enough that both can use the same guide stars, and (iii) the separation between the offset and target stars must be well known. The offset and target stars should be within 1.5 arcmin of each other. For the offset acquisitions, we chose GSC 6327-00161, a $V=15.5$ star that is 37.7 arcsec east and 87.4 arcsec south of the target star, GSC 6323-01396. These two stars are separated by 95.2 arcsec, just over the rough limit, but in this case neither guide stars nor gyro drift were a problem.

2.3 Adapting the Plan to the HST Scheduling Cycle

Even after planning all exposures for the observations, several tasks remain before the program is converted to instructions for the spacecraft. By 1991 Feb. 28 we had decided on GSC 6323-01396 as target for our first Guaranteed-Time Observer (GTO) occultation program, and we had updated the proposal except for the latest target position measurements. Astrometry of the two stars (GSC 6323-01396 and GSC 6327-00161) was performed at Wallace Astrophysical Observatory (Westford, MA), using the SNAPSHOT CCD in its strip-scanning mode (Dunham *et al.* 1985). For astrometric reference stars, we used the stars in the *HST Guide Star Catalog*, and reduced the data using the method described by Dunham *et al.* (1991). Because the acquisition planned was an offset acquisition, the important quantity was the *relative position* of the two stars. In order to assure accurate centering of the target star, its position relative to that of the offset star must be known to better than 0".1. In order to achieve this, we measured the positions of both stars on four strips. These new position measurements were submitted on 1991 Sept. 5, 27 days before the observation (less than the 90 days currently required).

At about 4–6 weeks before an observation, the Science Planning Branch (SPB) generates the first spacecraft ephemeris that covers the observing time in question. Using these, the SPB predicts the approximate observing windows (the time that occultation data can be recorded, constrained by Earth occultation, Earth bright-limb avoidance, solar and lunar avoidance, SAA passage, and target reacquisition). The average shift in observing windows over 6 weeks is approximately 10–15 min. Predictions made 4 weeks before the observation are more accurate, with an average shift of 2–3 min, but shifts of more than 5 min at this time are not uncommon.

Armed with these predictive windows, the SPB worked to schedule the occultation to fit into the windows. The scheduling process is normally handled automatically with computer code. In order to collect the maximum amount of data before and after SAA passages, large parts of the schedule were done by hand. We credit the schedulers with achieving the longest exposures within the SAA constraints, allowing us to record significantly more data than would have been possible with the automatic scheduling program.

2.4 Checking the Science Mission Schedule

A Science Mission Schedule (SMS) was produced, containing one week's worth of instructions for the instruments onboard the *HST*. As a last check before the science program was executed, we inspected the SMS for any errors on 1991 Sept. 12. We found that a spatial scan over Saturn and its rings would not be executed correctly, due to moving target support limitations. Part of the set of scans was to be executed within a single exposure [start data collection at the beginning of the first line, ending at the end of the last line with no breaks in data collection between lines; see Downes (1992) for a more complete explanation], but that capability had not yet been incorporated into the Moving Object Support System (MOSS). Although the single-exposure configuration is not a necessary factor, neither we nor the planners knew about the MOSS limitation until it failed during our SV test. As a

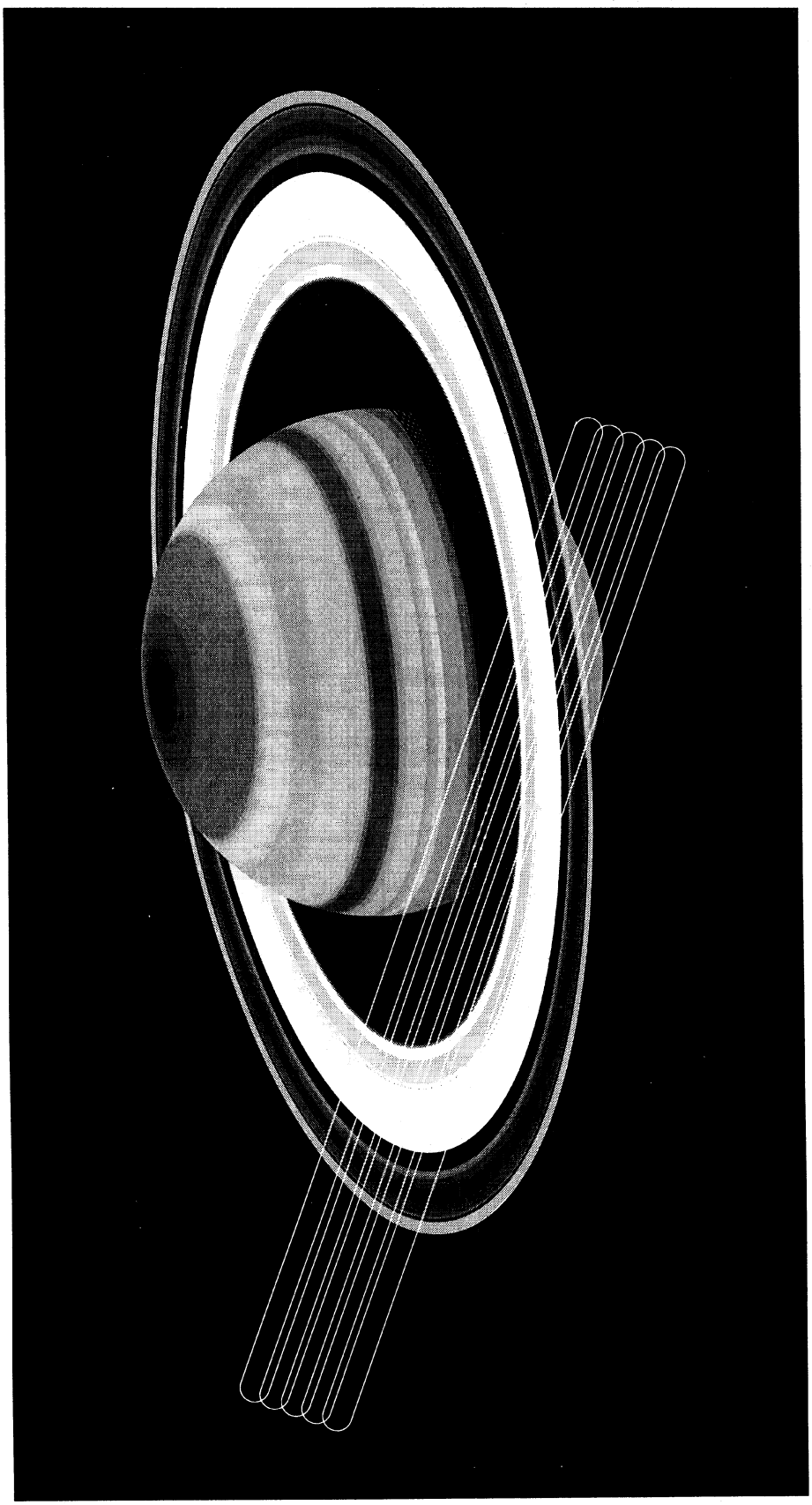

FIG. 2. Planned background scans, which encompass the overall track of GSC 6323-01396 relative to Saturn during the occultation. The stellar track is significantly distorted by spacecraft parallax (see Fig. 4), so a suite of overlapping background scans was planned to cover its entire path. Because of commanding difficulties, the multiple scan shown executed as a single pass, and an unanticipated time lag during telescope pointing led to incomplete and uncertain coverage of the length of the single track scanned.

TABLE 2. Exposure log.

Obs. ID[a]	Observation	Start Time (UTC)	Sample Time (s)	Exposure Time (s)
v0rr0101	Dark	1991 10 1 01 25 12.28[b]	0.15	288.0
v0rr0201	Back Scan	1991 10 1 19 40 43.29[b]	0.01	61.4
v0rr0202	Back Scan	1991 10 1 19 52 58.28[b]	0.15	777.6
v0rr0203	Back Scan	1991 10 1 21 00 57.29[b]	0.01	61.4
v0rr6301	Acquisition	1991 10 2 18 12 16.96[b]	0.30	120.0
v0rr6302	Acquisition	1991 10 2 18 18 10.96[b]	0.30	120.0
v0rr6401	Occ. Seg. 1	1991 10 2 19 35 10.5956	0.15	2419.2
v0rr6402	Occ. Seg. 2	1991 10 2 21 10 54.5955	0.15	518.4
v0rr6403	Occ. Seg. 3	1991 10 2 21 35 49.5955	0.15	979.2
v0rr6404	Occ. Seg. 4	1991 10 2 22 47 32.5957	0.15	633.6
v0rr6405	Occ. Seg. 5	1991 10 2 23 24 35.5948	0.15	199.5
v0rr6406	Occ. Seg. 6	1991 10 3 00 24 09.5956	0.15	777.6
v0rr6407	Occ. Seg. 7	1991 10 3 02 00 47.5957	0.15	1094.4
v0rr6408	Occ. Seg. 8	1991 10 3 03 37 24.5949	0.15	1468.8
v0rr6409	Occ. Seg. 9	1991 10 3 05 14 01.5958	0.15	1728.0
v0rr640a	Occ. Seg. 10	1991 10 3 06 50 39.5958	0.15	2188.8
v0rr640b	Occ. Seg. 11	1991 10 3 08 27 16.5959	0.15	2505.6
v0rr640c	Occ. Seg. 12	1991 10 3 10 03 54.5951	0.15	2505.6
v0rr640d	Occ. Seg. 13	1991 10 3 11 40 30.5949	0.15	2505.6
v0rr640e	Occ. Seg. 14	1991 10 3 13 17 08.5959	0.15	2505.6
v0rr640f	Occ. Seg. 15	1991 10 3 14 53 46.5969	0.15	2505.6
v0rr0501	Back Scan	1991 10 3 16 43 30.29[b]	0.01	61.4
v0rr0502	Back Scan	1991 10 3 16 55 45.28[b]	0.15	777.6
v0rr0503	Back Scan	1991 10 3 18 06 40.29[b]	0.01	61.4

Notes to TABLE 2

[a] Rootname of data set in HST Archive (Baum 1993).
[b] Indicated times do not include correction for spacecraft clock to UTC calibration, and are therefore approximate (by ~0.3 s).

result, the planned five-line scan would be executed as a single-line scan instead, scanning the middle of the apparent path only. This meant that we would lose valuable information about the ring background because we would not be scanning over the entire path followed by the star. However, we were not allowed to compensate for it by splitting the multiple-line scan into single-line scans because it was too close to the execution time. No other errors were detected in the SMS.

3. DATA

In contrast with ground-based and airborne occultation observations—where the most critical time for the observer is that just prior to and during the occultation—the observer has no duties during *HST* occultation observations: the die is cast with the final corrections to the SMS. By being present at the Observation Support System (OSS), we got a first look at the data coming in and noted the behavior of the spacecraft: the target acquisition was successful, and at times the guidance system suffered loss of lock (LOL). Although fine lock did not completely eliminate jitter, it vastly improved the quality of these data over those acquired in the SV test and enhanced the reliability of our feature measurements (described in Sec. 4). In this section we present the calibration and occultation data and discuss their properties.

3.1 Calibration Data

A list of all exposures for the data connected with this occultation is given in Table 2. The first exposures were "darks," for which the HSP aperture is trained on a dark region of sky and exposed for 5 min to ascertain the instrument noise level for both detectors (see Table 1). Although these exposures executed successfully, they identified a pre-existing limitation on data acquisition in our two-color mode which has since been rectified: although two separate detectors were used for our observations, their analog gains could not be set separately in star–sky mode of the HSP (Bless *et al.* 1993). Since the PMT and VIS detectors differ in sensitivity as well as wavelength, the relative signals received forced us to sacrifice potentially useful information from the analog format of the VIS detector in favor of the PMT.

As discussed above, our attempt to map the contribution of light from the rings to the total signal was thwarted by a previously unknown ground system restriction on single exposures in spatial scans. We had planned to scan back and forth across the planet and rings with the 1.0 arcsec aperture, with an offset of 0.75 arcsec between each

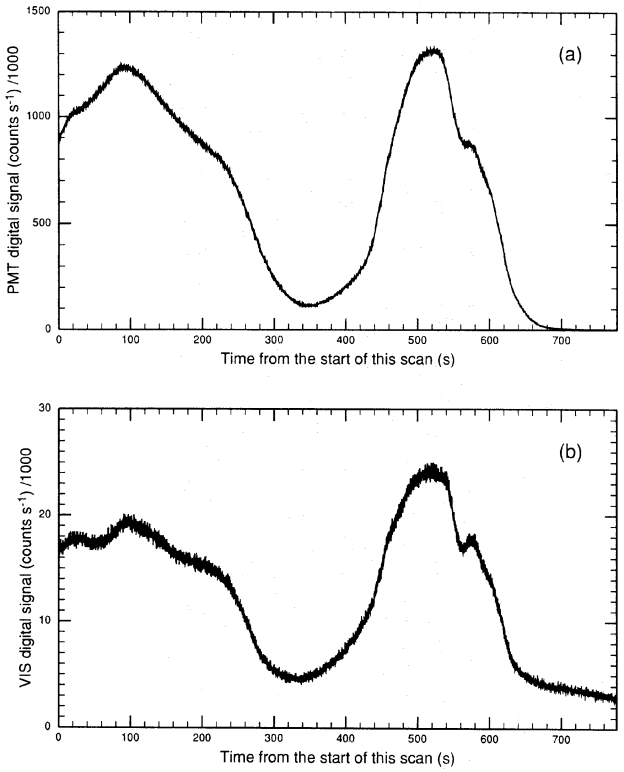

FIG. 3. A sample background scan from just southwest of the planet, across its bright face (interrupted by the rings and ring shadow), into the relatively empty (dark) space between planet and rings, and then outward through the ring system into dark sky, approximately along the path traced by the star as it was occulted by Saturn. Because of the uncertain timelag between the start of scanning and that of data collection, time is plotted relative to the start of this scan. Digital data are displayed from (a) photomultiplier tube (PMT, 7500 Å) and (b) image dissector tube (VIS, 3200 Å).

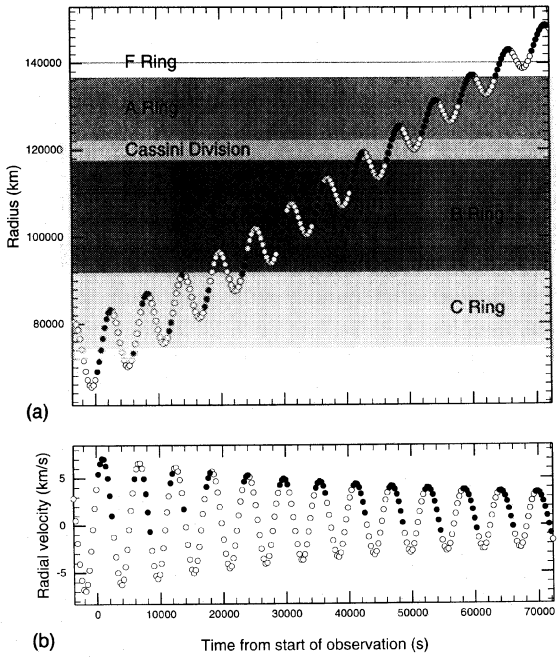

FIG. 5. (a) The variation of ring-plane radius with time, shown here with dots at 5 min intervals, is far from monotonic as the star moves generally outward in the rings. The portions of the track observed are indicated by the filled dots. (b) Variation of radial velocity (in the ring plane) with time during egress, at the same intervals as above. As the apparent stellar track nears its stationary point the radial velocity decreases to zero and then reverses sign as the *HST* rounds the limb of the Earth.

sweep (see Fig. 2). This restriction was discovered during the SV test, and thus the October observation was executed in the knowledge that the background would not be adequately mapped. An additional difficulty with background scans went unnoticed until data arrived. A timing problem that was masked by other problems in the SV test scans resulted in a significant uncertainty in the spatial coverage of the background scans. Commanding overhead delayed the onset of actual data collection within the scan intervals, thus both offsetting and reducing the scans' coverage of the Saturn-ring system. Since the background scans did not follow our planned raster, removal of the background from the occultation light curves will require considerable effort, and this task has not yet been attempted.

Figure 3 shows a sample background scan across the planet and rings, as recorded for each of the two photometric channels. The raw resolution of these background scans across Saturn and its rings is set by the smear of the HSP's 1.0 arcsec aperture (equivalent to 6000 km at the distance of Saturn). Although this is much larger than the few kilometer spatial resolution of the occultation data (see previous discussion, above) it can be improved through deconvolution.

3.2 Occultation Data

The apparent path of GSC 6323-01396 through Saturn's rings as seen by the *HST* is shown in Fig. 4 (Plate 110) with dots at 5 min intervals. Saturn was traveling southwest on the sky, so the star appeared to travel northeast relative to the planet. Two motions determine what parts of Saturn's rings are sampled by the star: parallax due to the orbital motion of the *HST*, and the relative motions of Saturn and the Earth. The former causes the apparent position of Saturn to move in a small ellipse relative to the star, and the latter stretches these ellipses out into the loops portrayed in the figure. The dependence of ring-plane radius and radial velocity on time due to these motions is shown in Fig. 5.

Data collection was not continuous as the star traced out this path. The spacecraft moved behind the Earth as seen from Saturn (the equivalent of Saturn setting for ground-based observers) for almost half of each 96 min orbit. Also, observations were precluded when the *HST* passed south of the equator over the Atlantic Ocean, through the SAA. Observation time was further reduced by the necessity to reacquire the guide stars following each of these interruptions, a process that takes about 5 min. The windows of observability are indicated in green in Fig. 4 and by the filled circles in Fig. 5.

The combined stellar and planetary flux was sampled at 0.15 s intervals by the two detectors at 3200 and 7500 Å, with both analog and digital data being recorded. For our

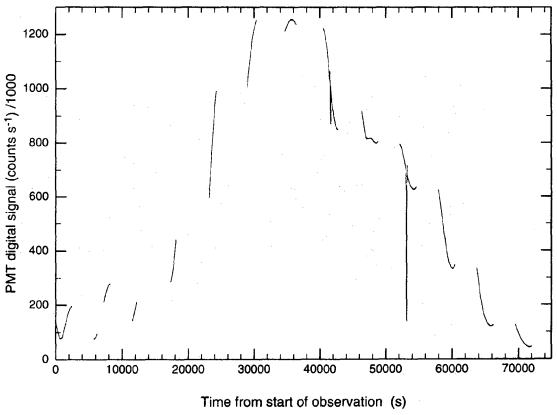

FIG. 6. Overview of the full occultation data set, fragmented by the visibility limitations discussed in the text (Earth occultations and SAA passages). The overall pattern is that of the bright Saturn-ring system convolved with the 1.0 arcsec aperture of the HSP, and the zigzag appearance is caused by parallax, the star moving in and out along its looping path relative to the varying ring background during each *HST* orbit. Most of the "glitches" on the smooth profile segments that can be seen at this scale are not ring features, rather they are episodes of loss of lock.

present goal of getting the most accurate times for ring-feature occultations, however, we treat only the digital signal from the photomultiplier tube (7500 Å), as it has a significantly higher signal-to-noise ratio (see Table 1). The 3200 Å digital data will not be used in this analysis.

An overview of the occultation light curve is shown in Fig. 6, fragmented by the visibility limitations imposed by Earth occultations and SAA passages. The overall pattern is that of the bright Saturn-ring system convolved with the 1.0 arcsec aperture of the HSP, and the zigzag appearance is caused by Saturn's parallax. The apparent position of the star moves along its helical path during each 96 min *HST* orbit; the apparent stellar path projected onto the ring plane traverses certain radial zones several times (see Fig. 5). A total of 6.8 h of occultation data were collected over a period of 20.0 h (covering 13 spacecraft orbits) during ring egress, for an "exposure efficiency" of 34 percent. The observation sequence spanned 65 h, including the acquisition of calibration and background data.

Most of the discontinuities on the smooth profile segments that can be seen at this scale are not ring features, but episodes of loss of lock (LOL). About 4 min after each day–night transition during the GSC 6323-01396 occultation observation, fine lock was sometimes seriously compromised or even lost. When lost, it was usually regained within a few minutes, as seen in Fig. 7. A LOL occurred, in fact, between the two onboard acquisitions of the offset star, but the second acquisition image was perfect nonetheless.

A typical case of pointing jitter and LOL incited just after day/night transition is shown in Fig. 7(a). Strong signal oscillations like those seen prior to total LOL can often be partially suppressed by smoothing the data [as in Fig. 7(c)] without seriously degrading the data content, but the star is well out of the aperture during LOL so the

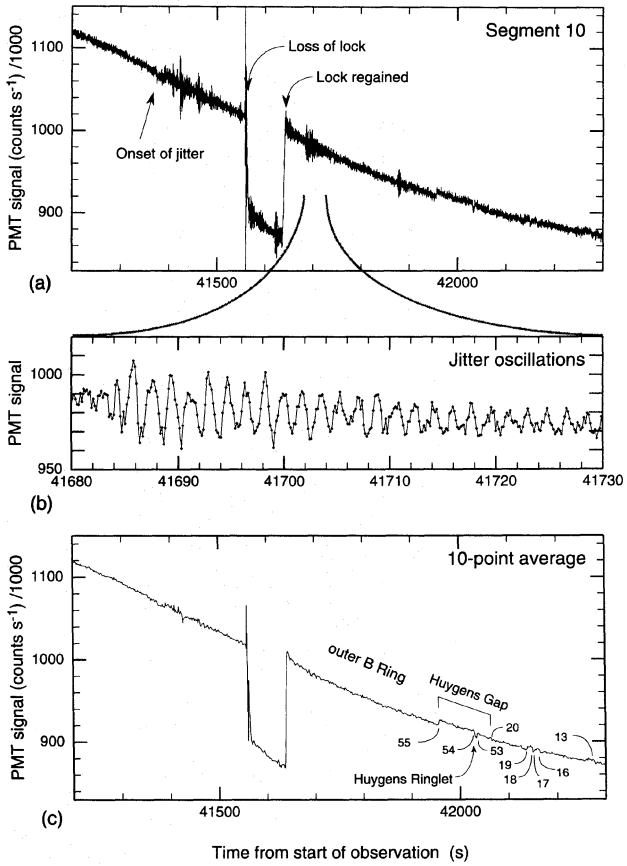

FIG. 7. PMT digital data for the tenth data segment, during which the telescope experienced jitter and loss of lock (LOL). (a) Full resolution, 0.15 s integrations. The star moving outward through the bright and optically thick outer B Ring at this time, so little if any of the fine-scale structure on the left of the plot is due to actual optical depth variations. On the right can be seen the outer edge of the B Ring, with the Huygens Gap and the inner Cassini Division. A few minutes after the *HST* passed into the Earth's shadow (orbital night), quasisinusoidal variations began in the received signal due to oscillations in telescope pointing across the strong background gradient. This effect can be seen expanded in (b), also at full resolution (open symbols mark each data point). Although the magnitude varies strongly, the frequency of the oscillation is fairly constant, about 0.7 Hz. Because of the jitter's regularity, much of its effect can be suppressed with moderate averaging. (c) A 10 point binned average of the light curve. Little of the jitter remains while the resulting 1.5 s resolution is adequate to unambiguously identify prominent ring features (labeled with feature number) once past the complete LOL.

data are useless until fine lock is recovered. Complete LOL occurred only three times during our observations, but episodes of jitter affected most of the data segments at least briefly.

The *HST* observation of this occultation began as the apparent position of the star was moving outward through the tenuous D ring, and continued as it traversed all of the classical C, B, and A rings and the F ring. The individual ring profile segments are shown in Fig. 8. In particular, several plateau regions in the C ring and the outer portion of the A ring (which contain the signatures of many satellite resonances) are each represented in two separate data segments at different azimuths.

Because of the orbital alignment of the *HST* at this time, all of the profile segments are approximately radial. In the

later segments, the stellar track goes through a maximum in ring-plane radius just before data collection is interrupted for Earth occultation. The radial component of the relative stellar velocity varies by more than an order of magnitude along each observed segment, so the effective radial sampling rate and the apparent noise level vary strongly [see Fig. 5(b)].

Normalized data segments are plotted against radius (with the parameters from our adopted geometric solution, discussed in Sec. 7) in Fig. 8. In order to view the light

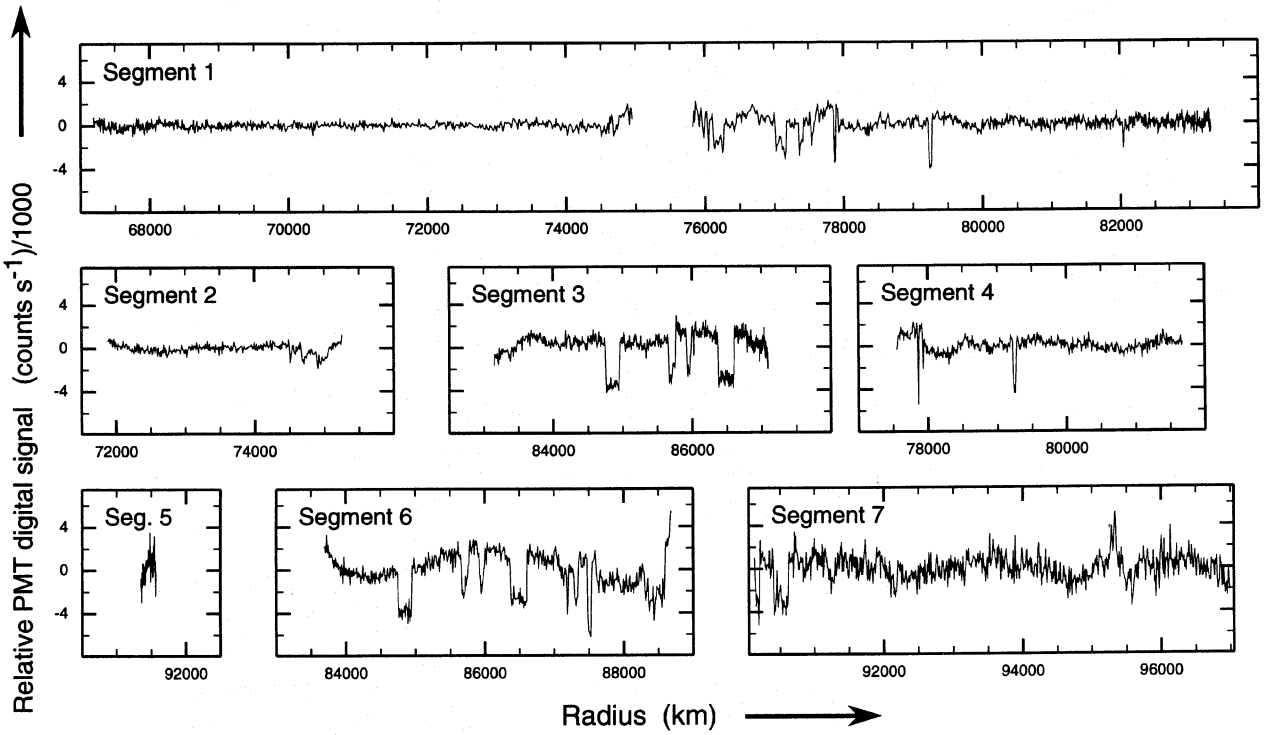

FIG. 8. The fifteen data segments of the occultation profile, shown at 1.5 s resolution (10 point binned averages) and plotted against radius in the ring plane. Although we have not been able to remove the true planetary background from the signal because of the commanding difficulties described in the text, in order to view the light curves on a reasonable scale we have filtered out the low frequency component of the profiles. Each segment has been detrended (subtracting a linear function in time so that both ends are at zero signal), and transformed into frequency space using an FFT algorithm. The lowest 1% of the frequencies were then transformed back into the time domain and subtracted from the detrended signal. Detrending of segments 11 and 14 was done with respect to the 100th point (rather than the first point) because of the strong increase in signal at the outer edges of the B and A rings, respectively. This process was performed in two parts for segments 1, 10, and 12, since LOL data were removed from these segments. Note also that because of SAA passages, the segments are not of uniform length. Many ring features are clearly discernible at this enhanced scale: (a) Segment 1: beginning interior to the main rings and moving outward through the variegated inner C Ring. Visible are features 44 (the inner edge of the C Ring), 40, 39, 63, and 62 (the Titan Ringlet), and 43 (the outer edge of the Titan Gap), 38, 37, 36. A mild episode of loss of lock (LOL) can be seen just before the ring edge crossing, but fortunately guidance had been recovered by the time the star passed behind the C Ring edge. (b) Segment 2: observation during this orbit was interrupted by an SAA passage, and with this segment the star just enters the innermost C Ring (crossing Feature 44 and its neighbors again). (c) Segment 3: the second observed portion of the same orbit as Segment 2 (after SAA passage), as the star moved from the middle into the outer C Ring. Features 35, 34, 33, 42, 31, 30, and 29 were traversed. (d) Segment 4: the first observed portion of the third orbit, covering the Titan Gap and Ringlet (features 63, 62, and 43) and the optical depth peak just outside it (edges 38 and 37). (e) Segment 5: a very short snippet at the other extreme of the third orbit, crossing no features. (f) Segment 6: although fairly brief, this segment spans the outer C Ring from the innermost plateau (features 35 and 34) out to the Maxwell Ringlet (61 and 60). (g) Segment 7: this segment runs from the outermost C Ring into the inner B Ring. (h) Segment 8: this segment covers many of the features in the B Ring (81 out through 71), though they can be difficult to identify and measure because of the high optical depth in the region and the possibility of noncircularity. (i) Segment 9: ring background brightness reaches a maximum during this segment, which contains probable identifications of features 72 and 71 in the middle B Ring. (j) Segment 10: the brightness of the aperture-smeared ring image decreased as the star moved outward in the B Ring; during this segment it crossed into the Cassini Division and features 55 (the outer edge of the B Ring), 54, 53, and 20 (the Huygens Ringlet and outer gap edge), and 19, 18, 17, 16, 13, and 15 are measured on this data segment. The prominent LOL (off-scale) is within the outer B Ring where there are no numbered features, so no measurements were compromised. (k) Segment 11: a second pass across the outer B Ring region, this time including the entire Cassini Division from feature 55 all the way out to feature 7. SAA passage is no longer interrupting observing time each orbit, so this and the remaining segments are the maximum length of almost 42 min, limited by Earth occultation and subsequent guide star reacquisition. These full-length segments (segments 11–15) also reach the extrema of the parallax-induced distortion, and the stellar track doubles back on itself. (l) Segment 12: spanned the inner and middle A Ring, where there are no distinct, numbered features. This episode of LOL (off-scale) thus had no serious effect on our feature measurements. (m) Segment 13: extends from the central A Ring out to the F Ring. Pointing jitter just outside the Encke Gap (features 4 and 3) is mostly suppressed by data averaging. (n) Segment 14: the Keeler Gap and the outer edge of the A Ring can be seen clearly near the left edge, but a probable F Ring feature detection is somewhat uncertain due to pointing jitter. (o) Segment 15: this entire segment is outside the main rings.

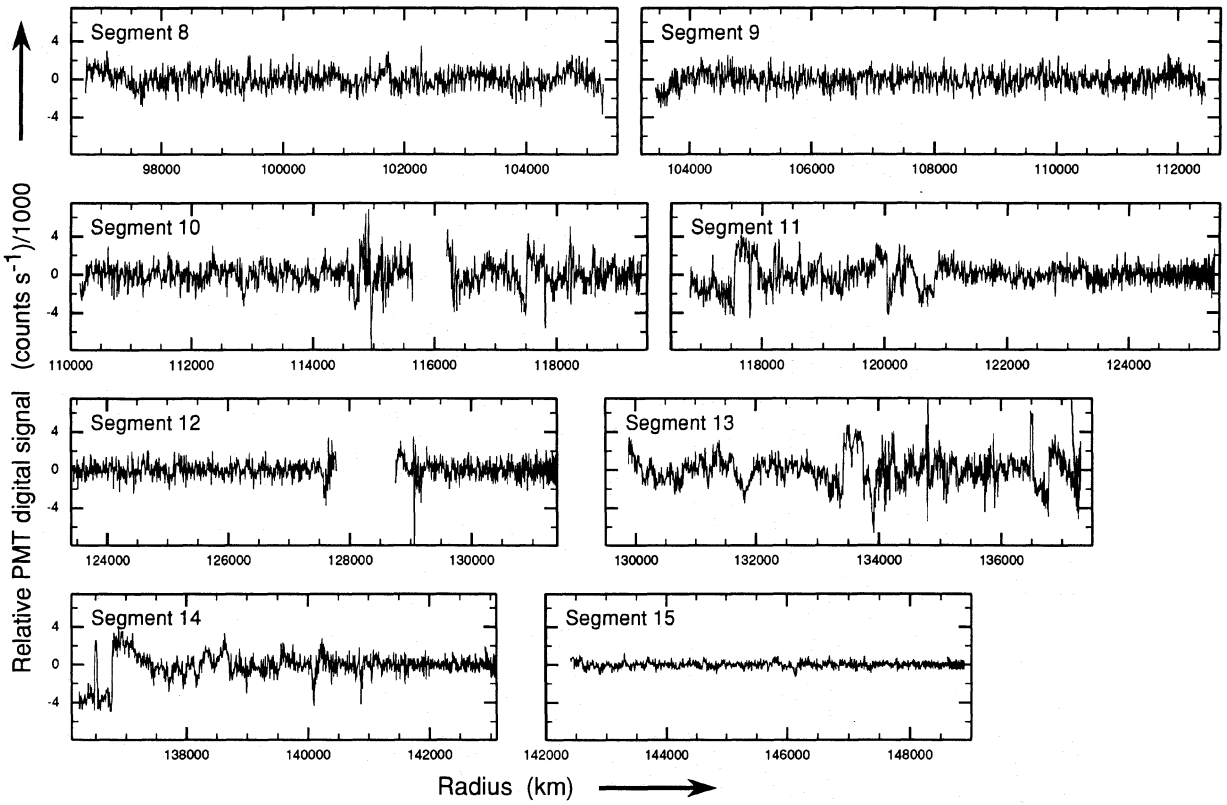

FIG. 8. (continued)

curves on a reasonable scale we have filtered out the low frequency component of the profiles. This filtering was done to remove the strong overall gradient in each segment, due to light from Saturn or its rings. We note that this filtering was performed only to aid in presentation; it is not a rigorous removal of background signal.

Some apparent azimuthal brightness variation is demonstrated by the relative background (ring) signal in multiple passages across the same radial regions as the telescope tracked the star (Fig. 9). This is likely due to a combination of foreshortening of the curved rings in the smeared image (which allows differing amounts of other regions to appear in the aperture) and the contribution of light reflected off the partially illuminated face of Saturn onto the rings: it highlights the necessity for detailed mapping of the background in future occultation observations. Another factor that may affect such differences between successive passages is the orbital variation in the system throughput that has become evident in other HSP observations (Bless *et al.* 1993).

3.3 Signal and Noise Levels

Because of the unfortunate lack of adequate background data, the best diagnostic within the data for determining the unocculted stellar signal received by our aperture is the light curve appearance near the Huygens Gap. This gap is basically empty, while the nearby B ring is almost opaque. The Titan, Maxwell, and Encke Gaps and the outer edge of the A ring provide similar stark transitions, but the ring optical depth is lower in those regions so appreciable stellar flux is transmitted outside the gaps. The stellar signal at the inner edge of the Huygens Gap is about 1050 detected photons per 0.15 s integration, or 7000 s^{-1} (about 0.5% of the full received signal in the B ring, and about 2% for the A ring; see Table 1). The measured rms noise is equivalent to 600 s^{-1} from the A ring for a 1.0 s integration, yielding a signal-to-noise ratio of 11 in 1.0 s. Although this signal-to-noise ratio is not as large as that for the best Earth-based observations of the 28 Sgr occultation (F93, Ha93, Hu93), it is entirely adequate for the purposes of measuring feature occultation times.

3.4 General Access to these Data

While these data are available in the *HST* Archives (Baum 1993), we intend to deposit them (along with ancillary information) in the Rings Node of the Planetary Data System (PDS), located at NASA Ames Research Center (M. R. Showalter, manager).

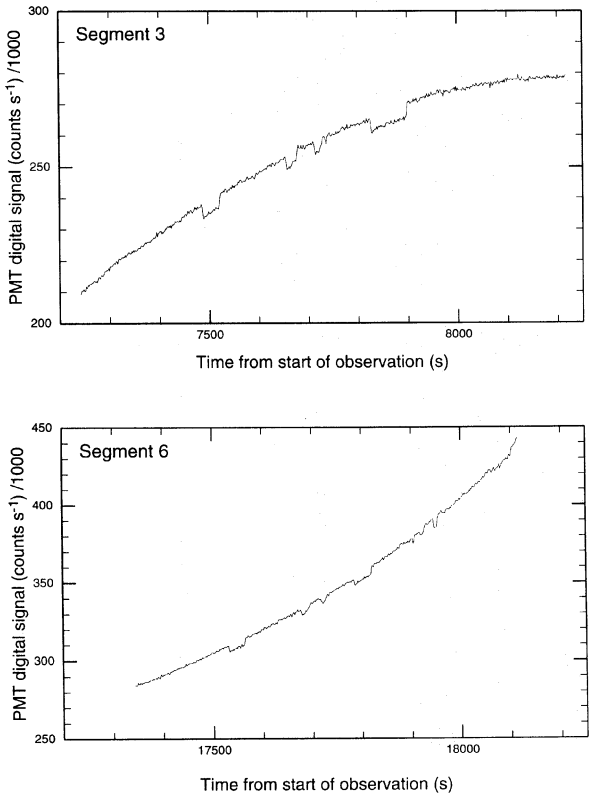

FIG. 9. Dual passages (during segments 3 and 6) of the star behind part of the outer C ring, a region characterized by sharp-edged, moderate optical depth ($0.3 < \tau < 0.5$) "plateaux" interspersed within a broad, low-optical depth "background." The strong overall gradients are the ring background; the differing curvature in the two profiles is due to the varying speed and curvature of the stellar track relative to the rings, as seen superposed on the synthetic ring "image" in Fig. 4, and is much reduced when a radial scale is applied. Note also the absolute difference in background signal between the two scans, despite similar radial coverage, indicating significant azimuthal brightness variation in the background, as discussed in the text.

4. FEATURE OCCULTATION TIMES

The signatures of many sharp optical-depth transitions in the rings are easily identified on the uncalibrated light curve, and several such features seen in two occultation segments are shown in Fig. 9. Ring features identified in the *HST* profile form a subset of those discussed by F93 and by Nicholson *et al.* (1990)—hereafter referred to as NCP. Not all of the features given in the catalog of F93 (see their Fig. 4) are included in our measurements, either because the feature was not covered by one of our light curve segments (we do not have a continuous radial profile), or because the optical depth change for the feature was not great enough to be apparent above the (radially variable) noise.

The first step in our analysis was to measure occultation times for the most prominent ring features in the uncalibrated profile. We used the "half-light" criterion employed by F93 for the definition of an edge. For a sharp edge, the "half-light" position for a monochromatic diffraction pattern would be shifted into the geometric shadow by 0.26 km for the 7500 Å channel. When the radial velocity is 8 km s^{-1}, however, the filtering imposed by the 0.15 s integration time reduces this shift to 0.15 km. Since "features" correspond to entering and exiting dense portions of ring material, this radial diffraction bias would tend to average out when these times are used in geometric models. Further evidence for the unimportance of diffraction effects in this data set relative to other data sets is that the signal to noise of these data is not sufficient to see diffraction fringes. For a radial velocity of 3 km s^{-1}, the main fringe for a sharp-edged opaque screen would have an amplitude of 1.28 if the phase of the integration bins relative to the edge crossing were optimized. Hence in the ideal case, detection of the main fringe would have an S/N of only 1.1; for the majority of real cases, however, the detectability would be less favorable.

The "half-light" times were incorporated into a first-generation geometrical model, and that solution was used to predict approximate event times for 104 possible crossings of features in the F93 catalog. The neighborhood of each of these predicted times was then examined, and times measured for those features that could be identified. This was done visually, since without accurate background calibration, the ring profile is superposed on a strongly varying baseline, which makes modeling difficult.

Of the 104 possible occultations (some multiple) by features in the F93 catalog, 18 fell just before or after the observed segment. About seven were probably traversed, but were either too difficult to detect in the data, or sufficiently noncircular that they fell outside the 30 s span of the search. Twelve features, mostly in the optically thick B ring or close to LOL jitter in the light curve, were identified as "probable." In some cases, intermediate refinements of the geometrical model using the full set of features enabled us to eliminate or improve ambiguous feature identifications (mostly in the B ring). This left 79 measured event times for feature crossings. These times are given in Table 3, along with an estimate of the certainty of identification. The estimated measurement uncertainties in the feature times range from 0.1 to 0.3 s (generally corresponding to less than 1 km radially), and these are also given in Table 3. Including only those features with confident identifications, we measure 67 event times. These correspond to 43 distinct features, with a second occultation by 24 of these.

Of our more confident identifications, many have been previously determined to be significantly noncircular (NCP,F93) and are thus not employed in our present model fits. Event times of the features that are currently presumed to be circular number 48 and are indicated in Table 4. Of these event times, 40 were identified with certainty, corresponding to 25 features presumed to be circular—15 features were occulted twice. These were the event times used in the geometric modeling.

5. MODEL FOR GEOMETRIC ANALYSIS

In order to interpret the occultation times for the features in Saturn's rings in terms of spatial coordinates

TABLE 3. Catalog of identified features.

Occ. Seg.	Feature ID[a]	Feature Radius[a]	Feature Time (after 1991 Oct. 2, 19:34:45.75 UTC)	Confidence Level[b]	Occ. Seg.	Feature ID[a]	Feature Radius[a]	Feature Time (after 1991 Oct. 2, 19:34:45.75 UTC)	Confidence Level[b]
1	44*	74490.76	968.52 ± 0.1	2	8	76	101002.53	29683.35 ± 0.2	1
1	40*	76263.93	1165.72 ± 0.1	2	8	74	101741.5	29811.79 ± 0.2	1
1	39*	77164.63	1269.13 ± 0.1	2	8	73	103009.2	30011.54 ± 0.3	1
1	63	77854.9	1351.27 ± 0.1	2	9	72	103657.03	34797.05 ± 0.2	1
1	62	77872.1	1353.01 ± 0.1	2	9	71	104087.19	34882.75 ± 0.2	1
1	43	77918.0	1358.69 ± 0.1	2	10	55	117516.0	41981.10 ± 0.1	2
1	38*	79220.31	1520.55 ± 0.1	2	10	54	117814.4	42055.70 ± 0.1	2
1	37*	79265.28	1526.12 ± 0.1	2	10	53	117833.7	42059.95 ± 0.1	2
1	36*	82040.58	1967.06 ± 0.1	2	10	20*	117932.25	42089.10 ± 0.1	2
2	44*	74490.76	6185.35 ± 0.1	2	10	19	118183.2	42162.65 ± 0.1	2
3	35*	84749.44	7510.15 ± 0.1	2	10	18	118229.3	42173.65 ± 0.1	2
3	34*	84949.38	7544.55 ± 0.1	2	10	17	118256.5	42177.60 ± 0.1	2
3	33*	85660.65	7680.30 ± 0.1	2	10	16*	118283.29	42188.45 ± 0.1	2
3	42*	85758.59	7701.55 ± 0.2	2	10	13*	118628.11	42300.65 ± 0.1	2
3	31*	85921.38	7736.90 ± 0.2	2	10	15*	118965.69	42434.35 ± 0.1	2
3	30*	86370.61	7851.15 ± 0.2	2	11	55	117516.0	46502.50 ± 0.1	2
3	29*	86601.11	7924.02 ± 0.1	2	11	54	117814.4	46551.85 ± 0.1	2
4	63	77854.9	11625.75 ± 0.1	2	11	53	117833.7	46555.75 ± 0.1	2
4	62	77872.1	11628.30 ± 0.1	2	11	20*	117932.25	46578.35 ± 0.1	1
4	43	77918.0	11638.15 ± 0.2	2	11	19	118183.2	46629.05 ± 0.1	2
4	38*	79220.31	11852.05 ± 0.1	2	11	18	118229.3	46636.25 ± 0.1	2
4	37*	79265.28	11858.35 ± 0.2	2	11	17	118256.5	46642.85 ± 0.1	2
6	35*	84749.44	17555.95 ± 0.2	2	11	16*	118283.29	46647.25 ± 0.1	2
6	34*	84949.38	17588.50 ± 0.1	2	11	13*	118628.11	46714.05 ± 0.2	2
6	33*	85660.65	17702.05 ± 0.1	2	11	15*	118965.69	46778.75 ± 0.2	2
6	42*	85758.59	17716.45 ± 0.1	2	11	14	120039.0	46983.35 ± 0.1	2
6	31*	85921.38	17742.05 ± 0.1	2	11	12*	120073.42	46988.85 ± 0.2	2
6	30*	86370.61	17809.45 ± 0.1	1	11	11*	120246.31	47023.05 ± 0.2	2
6	29*	86601.11	17843.55 ± 0.1	2	11	10	120305.7	47034.15 ± 0.1	2
6	61	87486.3	17969.95 ± 0.1	2	11	9	120316.5	47036.60 ± 0.1	2
6	60	87557.9	17977.75 ± 0.1	2	11	7*	122049.48	47383.30 ± 0.1	2
7	56	90197.3	23178.72 ± 0.1	2	13	4*	133423.53	58701.69 ± 0.1	2
7	24*	90404.08	23216.35 ± 0.1	2	13	3*	133745.14	58773.32 ± 0.1	2
7	23*	90614.87	23255.85 ± 0.2	2	13	2	136488.2	59521.29 ± 0.2	2
7	83	94439.46	23867.55 ± 0.2	1	13	1*	136522.28	59538.10 ± 0.1	2
7	82	95358.3	24004.05 ± 0.1	2	13	52	136774.4	59650.97 ± 0.1	2
7	81	96895.97	24235.50 ± 0.1	1	14	2	136488.2	63802.88 ± 0.1	2
8	81	96895.97	28993.72 ± 0.1	1	14	1*	136522.28	63813.15 ± 0.1	2
8	80	97212.9	29053.85 ± 0.3	1	14	52	136774.4	63867.42 ± 0.1	2
					14	51	140461.0	64612.25 ± 0.3	1

Notes to TABLE 3

[a]Feature ID and feature radius are after adopted solution of F93. Those features that are presumed circular and were included in our fits are marked with an asterisk; the radius values for known non-circular features are from F93 Table II.

[b]A value of "2" indicates a certain detection of this feature, while a value of "1" indicates a probable detection.

within the system, one must first construct the geometrical relation between the star, observer, and occulting planet. Approaches to this analysis have been developed to accommodate lunar and stellar occultations observed from Earth (Smart 1977; Elliot *et al.* 1978)—as well as stellar, solar, and radio occultations involving spacecraft (French *et al.* 1988; Holberg *et al.* 1987; Rosen *et al.* 1991a,b; NCP). Recently F93 have compared these geometrical methods in the context of reducing stellar occultation data for 28 Sgr and Saturn's rings. Their work uncovered numerous subtleties that depend on the coordinate systems and approximations chosen for the analysis, as well as errors at the few kilometer level (when used for Saturn ring occultation reductions) in computer codes that had been in use for many years (French *et al.* 1988). This lesson has underscored the importance of fully describing geometric methods used for analysis of occultation data.

5.1 Our Approach

Our method for combining *HST* and Earth-based occultation data employs a solar system barycentric reference system. One advantage of this approach is that the direction of the occulted star remains constant—at least to the

extent that its proper motion and stellar parallax can be neglected—so that one does not need to include differential stellar aberration. To simplify certain numerical calculations in our approach, however, we use a coordinate system centered on Saturn's shadow (cast in starlight) near the Earth and another centered on Saturn—a modification of the "sky-plane" method of Elliot *et al.* (1978).

Since our method does not include special relativistic effects, time and distance intervals will have inconsistencies that scale as $\sqrt{1-(v/c)^2}$, where v is the velocity of the planetary coordinate system relative to the solar system barycenter. For the velocity involved, this special relativity factor differs from unity by 5×10^{-9}. Hence the time interval between occultation and detection—about 10^4 s—would have inconsistencies at the 50 μs level (much smaller than our timing uncertainties for occultation features). The Earth–Saturn distance was about 1.5×10^9 km, so the distance inconsistencies would be about 8 km. Resultant errors in dimensions in the ring system, however, would be no more than 0.002 km (negligible for this work).

5.2 General Vector Equations

We begin the development of our method with vector equations describing the relationship between the positions of the occulting ring feature ("f"), planet center ("p"), barycenter of the planet–satellite system ("b"), Earth center ("e"), barycenter of the Earth–Moon system ("β"), and receiver ("r"). Some of these locations are illustrated by the vector diagram in Fig. 10. The main task of the geometric reduction is to derive the vector from the planet center to the occulting ring feature, $\mathbf{r}_{pf}$, that corresponds to the detection of the feature occultation at time t_r by the receiver (observer). This equals the difference between the vector from an arbitrary origin—in this case the solar system barycenter—to the ring feature, $\mathbf{r}_f$, and the vector from the same origin to the center of the planet, $\mathbf{r}_p$, at the time t_f when the feature occulted the star:

$$\mathbf{r}_{pf}(t_f)=\mathbf{r}_f(t_f)-\mathbf{r}_p(t_f). \tag{1}$$

Usually one must find the vector $\mathbf{r}_p(t)$ required by Eq. (1) from an ephemeris for the barycenter of the planet and its satellites, $\mathbf{r}_b(t)$. If $\mathscr{M}_p$ is the mass of the planet, $\mathscr{M}_j$ is the mass of the jth satellite, and $\mathbf{r}_{bj}(t)$ is the vector from the barycenter (of the planet and satellites) to the jth satellite, then we have

$$\mathbf{r}_p(t)=\mathbf{r}_b(t)-\sum_{j=1}^{\text{all satellites}}\frac{\mathscr{M}_j}{\mathscr{M}_p}\mathbf{r}_{bj}(t). \tag{2}$$

The feature occultation time occurs prior to its detection time by an amount equal to the light travel time between the feature and the receiver:

$$t_f=t_r-\frac{|\mathbf{r}_f(t_f)-\mathbf{r}_r(t_r)|}{c}. \tag{3}$$

This vector to the receiver, $\mathbf{r}_r(t)$, is derived from several ephemerides. For observations carried out in the vicinity of the Earth, the position of the receiver is the sum of two vectors, one to the Earth's center, $\mathbf{r}_e(t)$, another from the Earth's center to the receiver, $\mathbf{r}_{er}(t)$:

$$\mathbf{r}_r(t_r)=\mathbf{r}_e(t_r)+\mathbf{r}_{er}(t_r). \tag{4}$$

The vector to the Earth's center can be calculated from the vector to the Earth–Moon barycenter, $\mathbf{r}_\beta(t)$, the position of the Moon relative to the Earth, $\mathbf{r}_{em}(t)$, and the ratio of the mass of the Earth, $\mathscr{M}_e$, to the mass of the moon, $\mathscr{M}_m$:

$$\mathbf{r}_e(t_r)=\mathbf{r}_\beta(t_r)-\frac{1}{1+\mathscr{M}_e/\mathscr{M}_m}\mathbf{r}_{em}(t_r). \tag{5}$$

Having specified the positions of the planet and receiver, we proceed by adding and subtracting $\mathbf{r}_r(t_r)$ from the right-hand side of Eq. (1) and regrouping the terms for later convenience:

$$\mathbf{r}_{pf}(t_f)=\underbrace{[\mathbf{r}_f(t_f)-\mathbf{r}_r(t_r)]}_{\text{(i)}}-\underbrace{[\mathbf{r}_p(t_f)-\mathbf{r}_r(t_r)]}_{\text{(ii)}}. \tag{6}$$

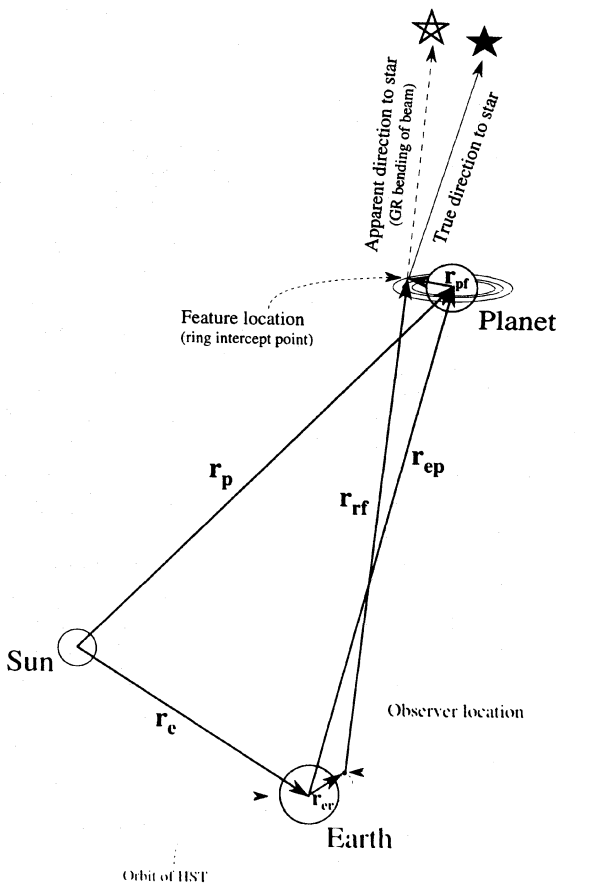

FIG. 10. Vectors used in our geometric model: $\mathbf{r}_e$ and $\mathbf{r}_p$, the geometric locations of Earth and the occulting planet from the solar-system barycenter (SSB); $\mathbf{r}_{er}$, the geocentric location of the observer (*HST*); $\mathbf{r}_{pf}$, the planetocentric location of an observed feature (such as a ring feature), and $\mathbf{r}_{rf}$, the vector from the observer to the feature as it is observed, i.e., along the apparent direction to the star, which differs from its real direction by a small angle due to gravitational bending of the beam by the occulting planet.

5.3 Planet-Plane Equations in the Solar-System Barycentric System

Next we further expand the terms of Eq. (6) in a manner that will facilitate numerical evaluation in the solar-system barycentric system. We define two parallel planes, each perpendicular to the unit vector to the star. The first plane passes through the receiver at time t_r, and we shall refer to it as the *shadow plane*. The second plane passes through the center of the planet at time t_π [defined in terms of t_r by Eq. (9) below], and we shall call this the *planet plane* (denoted by "π"). Note that the planet plane differs from the *sky plane*, which is defined by Elliot *et al.* (1978) to be perpendicular to the line of centers between the Earth and planet and passing through the planet's center. Also, the *fundamental plane* of Smart (1977) differs from our shadow plane in that the fundamental plane passes through the center of the Earth and is perpendicular to the line of centers between the Earth and planet.

Next we solve for several quantities that specify the geometric relationship of the planet plane and the receiver. We shall need the vector between the planet and receiver that intersects the planet center at time t_π and the receiver at time t_r. We denote this special "nonsimultaneous" vector by $\mathbf{r}_{rp}(t_r,t_\pi)$, and it is defined by the equation

$$\mathbf{r}_{rp}(t_r,t_\pi)\equiv\mathbf{r}_p(t_\pi)-\mathbf{r}_r(t_r). \tag{7}$$

The perpendicular distance between the receiver and the planet plane, $d_{r\pi}(t_r,t_\pi)$, is given by the projection of this vector onto the direction to the star, $\hat{\mathbf{r}}_s$:

$$d_{r\pi}(t_r,t_\pi)=\mathbf{r}_{rp}(t_r,t_\pi)\cdot\hat{\mathbf{r}}_s. \tag{8}$$

Knowing this distance, we can compute the time t_π as the difference between the received time and the light-travel time between the planet plane and receiver:

$$t_\pi=t_r-\frac{d_{r\pi}(t_r,t_\pi)}{c}. \tag{9}$$

The relationship between these times is shown on the timeline of Fig. 11. To find $\mathbf{r}_{rp}(t_r,t_\pi)$, $d_{r\pi}(t_r,t_\pi)$, and t_π, we must perform an iterative, simultaneous solution of Eqs. (7), (8), and (9). This completes the specification of the planet plane in terms of the observed feature occultation time, t_r, and the geometric ephemerides for the planet and receiver.

5.4 Remaining Vector Equations for Feature Radii

Our approach will be to express occultation geometry in terms of solutions that would apply if the occulting feature were in the planet plane and then to correct for the position of the feature relative to this plane. First we expand term (i) of Eq. (6). This vector lies in the apparent direction of the star (as affected by the general relativistic bending of starlight) and has a length $d_{r\pi}(t_r,t_\pi)+d_{\pi f}(t_r)$, where $d_{\pi f}(t_r)$ is the perpendicular distance between the feature and the planet plane:

$$\mathbf{r}_{rf}(t_r,t_f)\equiv\mathbf{r}_f(t_f)-\mathbf{r}_r(t_r), \tag{10}$$

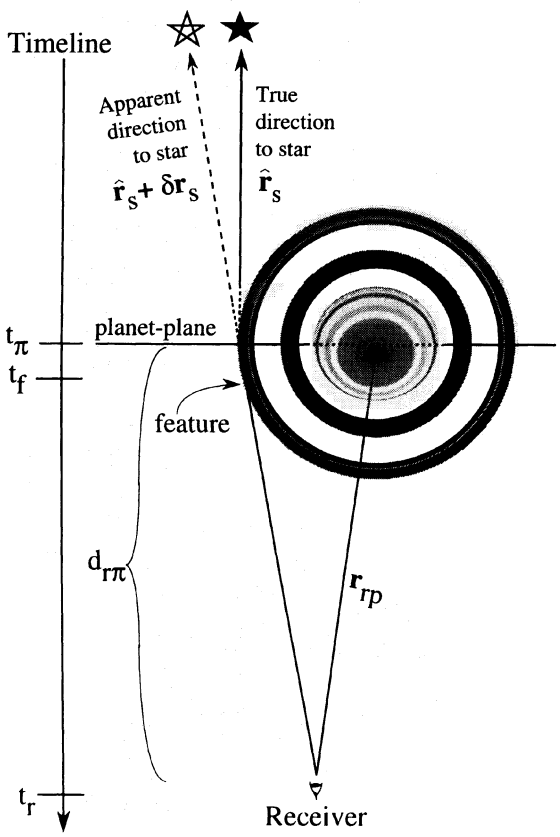

FIG. 11. Nonsimultaneous vector $\mathbf{r}_{rp}(t_r,t_\pi)$, illustrating the backdated times used in the geometric model. The planet position is calculated first at the time t_π, and this position is then corrected for the difference between t_π and t_f. The solar-system barycentric velocity of the planet is used in this calculation.

$$d_{\pi f}(t_r)=\mathbf{r}_{rf}(t_r,t_f)\cdot\hat{\mathbf{r}}_s-d_{r\pi}(t_r,t_\pi). \tag{11}$$

The direction to the star in the solar system barycentric frame is the sum of a unit vector, $\hat{\mathbf{r}}_s$, and a small correction term, $\delta\mathbf{r}_s$, due to the general relativistic bending of starlight by the gravitational field of the planet. The error introduced by approximating the bending effect of general relativity by an abrupt change of direction at the planet rather than the actual curved path is extremely small and therefore ignored. With these definitions, we write term (i) of Eq. (6) differently in two domains. The first domain applies when the feature is closer to the receiver than the planet plane, and the second applies when the feature is further. For $|\delta\mathbf{r}_s|\ll 1$,

$$\mathbf{r}_f(t_f)-\mathbf{r}_r(t_r)=\begin{cases}[d_{r\pi}(t_r,t_\pi)+d_{\pi f}(t_r)](\hat{\mathbf{r}}_s+\delta\mathbf{r}_s), & t_f\geqslant t_\pi,\\ [d_{r\pi}(t_r,t_\pi)+d_{\pi f}(t_r)]\hat{\mathbf{r}}_s+d_{r\pi}(t_r,t_\pi)\delta\mathbf{r}_s, & t_f<t_\pi.\end{cases} \tag{12}$$

The difference between these two cases, $d_{\pi f}(t_r)\delta\mathbf{r}_s$, amounts to less than 0.003 km for the present analysis—a small fraction of the 30 km deflection that would be experienced by a ray passing tangent to the limb of Saturn.

Since the second expression is more convenient algebraically, we shall always use it, independent of whether the feature is closer or further from the receiver than the planet plane.

In summary, we have made four approximations in our treatment of general relativity: (i) the bending occurs at a point, (ii) the second form of Eq. (12) is used even when $t_f \geqslant t_\pi$, (iii) $|\hat{\mathbf{r}}_s + \delta\mathbf{r}_s| \approx 1$, and (iv) $\mathbf{v}\cdot\hat{\mathbf{r}}_s \approx \mathbf{v}\cdot(\hat{\mathbf{r}}_s + \delta\mathbf{r}_s)$, where $\mathbf{v}$ is any vector. None of these approximations results in errors larger than a few meters for the present analysis.

Next we expand term (ii) of Eq. (6). We have previously defined t_π as the time that the occulted light arrives at the planet plane and, using our convention for "nonsimultaneous" vectors, we denote the difference in the vector $\mathbf{r}_p$ between the times t_f and t_π by $\mathbf{r}_{pp}(t_f,t_\pi)$, so that

$$\mathbf{r}_{pp}(t_f,t_\pi) = \mathbf{r}_p(t_\pi) - \mathbf{r}_p(t_f). \tag{13}$$

We can now write term (ii) of Eq. (6) as

$$\begin{aligned}\mathbf{r}_p(t_f) - \mathbf{r}_r(t_r) &= \mathbf{r}_p(t_\pi) - \mathbf{r}_r(t_r) - \mathbf{r}_{pp}(t_f,t_\pi),\\ &= \mathbf{r}_{rp}(t_r,t_\pi) - \mathbf{r}_{pp}(t_f,t_\pi).\end{aligned} \tag{14}$$

We substitute the expressions in Eqs. (12) and (14) for the corresponding terms in Eq. (6) and rearrange them into an order convenient for numerical evaluation. We find

$$\mathbf{r}_{pf}(t_f) = \underbrace{-\mathbf{r}_{rp}(t_r,t_\pi)}_{\#1} + \underbrace{[d_{r\pi}(t_r,t_\pi) + d_{\pi f}(t_r)]\hat{\mathbf{r}}_s}_{\#2} + \underbrace{\mathbf{r}_{pp}(t_f,t_\pi)}_{\#3} + \underbrace{d_{r\pi}(t_r,t_\pi)\delta\mathbf{r}_s}_{\#4}. \tag{15}$$

Our next task will be to convert each of the terms in Eq. (15) to an algebraic form that will be suitable for numerical evaluation with available ephemerides for the near-Earth receiver and the planet (*HST* and Saturn in this case). To do this, we must first define appropriate coordinate systems.

5.5 Coordinate Systems

We begin with the J2000.0 *XYZ* rectangular coordinate system (USNO 1992). In this system we specify the coordinates of a body at $\mathbf{r}$ either by its X, Y, and Z components, or by its distance from a specified origin (such as the center of the Earth) and its right ascension and declination, α and δ, respectively. The right ascension and declination are defined in terms of the projection of the unit vector $\hat{\mathbf{r}}$ to the body onto the unit vectors of the J2000.0 system, $\hat{\mathbf{X}}$, $\hat{\mathbf{Y}}$, and $\hat{\mathbf{Z}}$:

$$\begin{aligned}\cos\alpha\cos\delta &= \hat{\mathbf{r}}\cdot\hat{\mathbf{X}},\\ \sin\alpha\cos\delta &= \hat{\mathbf{r}}\cdot\hat{\mathbf{Y}},\\ \sin\delta &= \hat{\mathbf{r}}\cdot\hat{\mathbf{Z}}.\end{aligned} \tag{16}$$

Next we set up an *fgh* coordinate system in the shadow plane that originates at the center of the planet's shadow, with $\hat{\mathbf{f}}$ pointing in the direction of increasing right ascension. The axis $\hat{\mathbf{h}}$ lies in the direction of the star, $\hat{\mathbf{r}}_s$. Formally, the unit vectors of the *fgh* system are

$$\begin{aligned}\hat{\mathbf{f}} &= \frac{\hat{\mathbf{Z}}\times\hat{\mathbf{r}}_s}{|\hat{\mathbf{Z}}\times\hat{\mathbf{r}}_s|},\\ \hat{\mathbf{g}} &= \hat{\mathbf{r}}_s\times\frac{\hat{\mathbf{Z}}\times\hat{\mathbf{r}}_s}{|\hat{\mathbf{Z}}\times\hat{\mathbf{r}}_s|},\\ \hat{\mathbf{h}} &= \hat{\mathbf{r}}_s.\end{aligned} \tag{17}$$

We define another rectangular coordinate system—*uvw*—centered on the planet, with the w axis pointed in the direction of the star. The u axis is parallel to the major axes of apparent ring ellipses as seen from the geocenter, and the v axis is parallel to the minor axes of the apparent ring ellipses. The unit vectors of the *uvw* system are:

$$\begin{aligned}\hat{\mathbf{u}} &= \frac{\hat{\mathbf{r}}_n\times\hat{\mathbf{r}}_s}{|\hat{\mathbf{r}}_n\times\hat{\mathbf{r}}_s|},\\ \hat{\mathbf{v}} &= \hat{\mathbf{r}}_s\times\frac{\hat{\mathbf{r}}_n\times\hat{\mathbf{r}}_s}{|\hat{\mathbf{r}}_n\times\hat{\mathbf{r}}_s|},\\ \hat{\mathbf{w}} &= \hat{\mathbf{r}}_s.\end{aligned} \tag{18}$$

Finally we define an *xyz* coordinate system centered on the planet, with the z axis coincident with the north pole of the planet's ring plane, $\hat{\mathbf{r}}_n$. The x axis is the intersection of the planet's equatorial plane with the Earth's equatorial plane (J2000.0), with the positive portion at the ascending node for prograde revolution. The unit vectors defining the axes are:

$$\begin{aligned}\hat{\mathbf{x}} &= \frac{\hat{\mathbf{Z}}\times\hat{\mathbf{r}}_n}{|\hat{\mathbf{Z}}\times\hat{\mathbf{r}}_n|},\\ \hat{\mathbf{y}} &= \hat{\mathbf{r}}_n\times\frac{\hat{\mathbf{Z}}\times\hat{\mathbf{r}}_n}{|\hat{\mathbf{Z}}\times\hat{\mathbf{r}}_n|},\\ \hat{\mathbf{z}} &= \hat{\mathbf{r}}_n.\end{aligned} \tag{19}$$

In order to give the elements of the rotation matrices that are used to transform from one system to another, we define three auxiliary angles: B_s, the angle between the north pole of the planet and the fg plane ($-\pi/2 \leqslant B_s \leqslant \pi/2$); P_s, the position angle of the projection of the north pole of the planet onto the fg plane, and U_s, the longitude of the projection of $\hat{\mathbf{h}}$ into the xy plane ($0 \leqslant P_s$, $U_s < 2\pi$). We use the subscript "s" to remind us that these angles are defined in terms of the star position, rather than the usual definition in terms of the position of the planet. P_s is measured $\hat{\mathbf{g}}\rightarrow\hat{\mathbf{f}}$, and U_s is measured $\hat{\mathbf{x}}\rightarrow\hat{\mathbf{y}}$. These angles can be expressed in terms of the celestial coordinates of the star and north pole of the planet:

$$\begin{aligned}\sin B_s &= -\hat{\mathbf{h}}\cdot\hat{\mathbf{z}}\\ &= -\hat{\mathbf{r}}_n\cdot\hat{\mathbf{r}}_s = -\sin\delta_n\sin\delta_s\\ &\quad -\cos\delta_n\cos\delta_s\cos(\alpha_s-\alpha_n),\end{aligned} \tag{20}$$

$$\begin{aligned}\cos B_s \cos P_s &= \hat{\mathbf{g}}\cdot\mathbf{z}\\ &= \sin\delta_n\cos\delta_s\\ &\quad -\cos\delta_n\sin\delta_s\cos(\alpha_s-\alpha_n),\\ \cos B_s \sin P_s &= \hat{\mathbf{f}}\cdot\hat{\mathbf{z}} = -\cos\delta_n\sin(\alpha_s-\alpha_n),\end{aligned} \tag{21}$$

$$\begin{aligned}\cos B_s \cos U_s &= \hat{\mathbf{x}}\cdot\hat{\mathbf{w}} = \cos\delta_s\sin(\alpha_s-\alpha_n),\\ \cos B_s \sin U_s &= \hat{\mathbf{y}}\cdot\hat{\mathbf{w}}\\ &= \sin\delta_s\cos\delta_n - \cos\delta_s\sin\delta_n\cos(\alpha_s-\alpha_n).\end{aligned} \tag{22}$$

Next we write expressions for the rotation matrices needed to convert vectors between the *XYZ*, *fgh*, *uvw*, and *xyz* coordinate systems. If α_s and δ_s are the right ascension and declination of the star, defined by equations analogous to Eq. (16), then the rotation matrix for converting a vector to *fgh* from *XYZ*, J2000.0 is $\mathbf{R}_{XYZ\rightarrow fgh}$ and is given by

$$\begin{aligned}\mathbf{R}_1 &\equiv \mathbf{R}_{XYZ\rightarrow fgh}\\ &= \begin{bmatrix}\hat{\mathbf{f}}\cdot\hat{\mathbf{X}} & \hat{\mathbf{f}}\cdot\hat{\mathbf{Y}} & \hat{\mathbf{f}}\cdot\hat{\mathbf{Z}}\\ \hat{\mathbf{g}}\cdot\hat{\mathbf{X}} & \hat{\mathbf{g}}\cdot\hat{\mathbf{Y}} & \hat{\mathbf{g}}\cdot\hat{\mathbf{Z}}\\ \hat{\mathbf{h}}\cdot\hat{\mathbf{X}} & \hat{\mathbf{h}}\cdot\hat{\mathbf{Y}} & \hat{\mathbf{h}}\cdot\hat{\mathbf{Z}}\end{bmatrix}\\ &= \begin{bmatrix}-\sin\alpha_s & \cos\alpha_s & 0\\ -\cos\alpha_s\sin\delta_s & -\sin\alpha_s\sin\delta_s & \cos\delta_s\\ \cos\alpha_s\cos\delta_s & \sin\alpha_s\cos\delta_s & \sin\delta_s\end{bmatrix}.\end{aligned} \tag{23}$$

The rotation matrix for converting the *f* and *g* components in the shadow plane to its *u* and *v* components in the planet plane is

$$\mathbf{R}_2 \equiv \mathbf{R}_{fg\rightarrow uv} = \begin{bmatrix}\hat{\mathbf{u}}\cdot\hat{\mathbf{f}} & \hat{\mathbf{u}}\cdot\hat{\mathbf{g}}\\ \hat{\mathbf{v}}\cdot\hat{\mathbf{f}} & \hat{\mathbf{v}}\cdot\hat{\mathbf{g}}\end{bmatrix} = \begin{bmatrix}\cos P_s & -\sin P_s\\ \sin P_s & \cos P_s\end{bmatrix}. \tag{24}$$

We shall also use the inverse of $\mathbf{R}_2$, $\mathbf{R}_2^{-1}$, to convert from the planet plane to shadow plane.

The rotation matrix for conversion from *uvw* coordinates to the *xyz* system, $\mathbf{R}_{uvw\rightarrow xyz}$, is given by

$$\begin{aligned}\mathbf{R}_3 &\equiv \mathbf{R}_{uvw\rightarrow xyz}\\ &= \begin{bmatrix}\hat{\mathbf{x}}\cdot\hat{\mathbf{u}} & \hat{\mathbf{x}}\cdot\hat{\mathbf{v}} & \hat{\mathbf{x}}\cdot\hat{\mathbf{w}}\\ \hat{\mathbf{y}}\cdot\hat{\mathbf{u}} & \hat{\mathbf{y}}\cdot\hat{\mathbf{v}} & \hat{\mathbf{y}}\cdot\hat{\mathbf{w}}\\ \hat{\mathbf{z}}\cdot\hat{\mathbf{u}} & \hat{\mathbf{z}}\cdot\hat{\mathbf{v}} & \hat{\mathbf{z}}\cdot\hat{\mathbf{w}}\end{bmatrix}\\ &= \begin{bmatrix}-\sin U_s & \sin B_s\cos U_s & \cos B_s\cos U_s\\ \cos U_s & \sin B_s\sin U_s & \cos B_s\sin U_s\\ 0 & \cos B_s & -\sin B_s\end{bmatrix}.\end{aligned} \tag{25}$$

We conclude this section by noting that the direction to the ring-plane pole may vary with time, due to planetary precession. For the time scales of interest here, we can approximate this precession by its linear terms in right ascension and declination. If $\dot{\alpha}_n$ is the rate of polar motion in right ascension, $\dot{\delta}_n$ the rate of polar motion in declination, and t_n the reference epoch for the position of the pole, then we have

$$\begin{aligned}\alpha_n &= \alpha_n(t) = \alpha_n(t_n) + \dot{\alpha}_n(t-t_n),\\ \delta_n &= \delta_n(t) = \delta_n(t_n) + \dot{\delta}_n(t-t_n).\end{aligned} \tag{26}$$

Similarly, if the occulted star exhibits significant proper motion, we could introduce this in an analogous manner.

5.6 Corrections to Time and Positions

When evaluating the terms in Eq. (15) to find the feature radius, we find that all are not readily available, so we must write these terms as functions of the information we actually use to reduce the data. In this section we consider three correction terms that improve the connection of our model to the time and position measurements used for the data reduction. The effects included are: (i) a constant offset between the planetary ephemeris and the actual planetary position; (ii) a difference between the catalog star position and the actual star position; and (iii) a constant offset between the time scale used as the argument for the occultation light curve (e.g., *HST* clock) and UTC. An example of an effect not considered in our model is an error in the *HST* ephemeris. (To a great extent, however, an in-track error in the *HST* ephemeris would mimic an error in the *HST* clock.)

To evaluate the effect produced by a difference between the ephemeris position of the planet and its actual position, we define a vector $\mathbf{r}_{pp'}(t_f)$ that represents the difference between the ephemeris position and the planetary position

$$\mathbf{r}_{pp'}(t_f) \equiv \mathbf{r}_{p'}(t_f) - \mathbf{r}_p(t_f). \tag{27}$$

If we assume that this error is a constant offset, then

$$\mathbf{r}_{pp'}(t_f)\,|_{fgh} \equiv \begin{bmatrix}f_o\\ g_o\\ h_o\end{bmatrix} = \mathbf{R}_1\mathbf{r}_{pp'}(t_f)\,|_{XYZ} = \mathbf{R}_1\begin{bmatrix}X_{pp'}\\ Y_{pp'}\\ Z_{pp'}\end{bmatrix}. \tag{28}$$

Analogously, we define $\hat{\mathbf{r}}_{ss'}$ as the difference between the catalog star position, $\hat{\mathbf{r}}_{s'}$, and actual star position, $\hat{\mathbf{r}}_s$. It will be convenient to express the difference as offsets in right ascension, α_o, and declination, δ_o:

$$\begin{aligned}\alpha_s &= \alpha_{s'} - \alpha_o,\\ \delta_s &= \delta_{s'} - \delta_o.\end{aligned} \tag{29}$$

Finally we allow the clock time used for the data recording, t_c, to have a constant offset, t_o, from the desired time in UTC, *t*:

$$t = t_c - t_o. \tag{30}$$

The implication of Eq. (30) is that all feature occultation times taken from the light curve are shifted by t_o.

5.7 Evaluation of Sky-Plane Terms

For the terms in Eq. (15), we know (or can calculate from known quantities) the planet-plane coordinates of the

occulting ring feature, but not the coordinate perpendicular to this plane, $w_f(t_f)$. However, we shall be modeling the occulting features as circular rings, lying in the equatorial plane of the planet. This will allow us to determine $w_f(t_f)$ from planet-plane coordinates of the feature and the direction of the planet's ring-plane pole. So our plan for evaluation is as follows: (i) evaluate the fg components of the terms in Eq. (15), (ii) project the fg components from the shadow plane to the planet-plane to find the uv components of the occulting feature (this procedure involves only the correction for general relativity bending), (iii) assume the occulting feature lies in the equatorial plane of the planet, and find w from the planet-plane coordinates, and (iv) convert uvw to xyz from which we calculate the feature longitude and radius.

Except for term #1 given by Eq. (15), we require prior knowledge of $w_f(t_f)$ for evaluation, so we must resort to an iterative procedure in order to arrive at a solution. For our iteration procedure we begin with the loop index $i=1$, and for the ith iteration we denote the value of a quantity q by $q_{(i)}$. We begin with the prior value $w_{f(0)}=0$. Then we find the distance between the occulting feature and planet plane. Within our approximations for general relativity, this lies along the w axis:

$$d_{\pi f(i)}(t_r)=w_{f(i-1)}(t_f). \tag{31}$$

Knowing the light travel distance, we can now calculate the feature occultation time, $t_{f(i)}$:

$$t_{f(i)}=t_\pi-\frac{d_{\pi f(i)}(t_r)}{c}. \tag{32}$$

Now we can find the f and g components of term #3 of Eq. (15), the light travel correction from the feature to the planet center. We calculate these from the solar-system barycentric velocity of the planet (including effects of its satellite motions) [$\dot{X}_p(t_\pi)$, $\dot{Y}_p(t_\pi)$, and $\dot{Z}_p(t_\pi)$], using a linear approximation

$$\mathbf{r}_{pp(i)}(t_f,t_\pi)\,|_{fgh}=\begin{bmatrix} f_{pp(i)}(t_f,t_\pi)\\ g_{pp(i)}(t_f,t_\pi)\\ h_{pp(i)}(t_f,t_\pi)\end{bmatrix}$$

$$=(t_\pi-t_{f(i)})\mathbf{R}_1\begin{bmatrix}\dot{X}_p(t_\pi)\\ \dot{Y}_p(t_\pi)\\ \dot{Z}_p(t_\pi)\end{bmatrix}. \tag{33}$$

We can now write complete equations for the f and g coordinates of the feature. The terms have been grouped in the equations below according to their parent terms in Eq. (15):

$$f_{pf(i)}(t_r)=-\underbrace{[f_{rp'}(t_r,t_\pi)-f_o]}_{\#1}+\underbrace{f_{pp(i)}(t_f,t_\pi)}_{\#3}+\underbrace{f_{s(i)}(t_\pi)}_{\#4}, \tag{34}$$

$$g_{pf(i)}(t_r)=-\underbrace{[g_{rp'}(t_r,t_\pi)-g_o]}_{\#1}+\underbrace{g_{pp(i)}(t_f,t_\pi)}_{\#3}+\underbrace{g_{s(i)}(t_\pi)}_{\#4}. \tag{35}$$

In order to evaluate Eqs. (34) and (35) we need an expression for the general relativity bending terms, $f_{s(i)}(t_\pi)$ and $g_{s(i)}(t_\pi)$. Finding these requires a second iterative loop, internal to the first. The general relativistic bending equations correct to second order are given by Hu93 [their Eqs. (13)–(14)]. First we define $r_{f,uv}$ as the radius of the occulting feature, projected into the planet plane:

$$r_{f,uv(i)}(t_f)=\sqrt{u^2_{f(i)}(t_f)+v^2_{f(i)}(t_f)}. \tag{36}$$

In the equations below, J_2 is the coefficient of the second-order gravitational harmonic and R_p is the equatorial radius of the planet. Using Eqs. (13) and (14) of Hu93, we write the equations for the general relativity bending in our notation:

$$\begin{bmatrix} f_{s(i)}(t_f)\\ g_{s(i)}(t_f)\end{bmatrix}=\frac{4G\mathscr{M}_p d_{r\pi}(t_r,t_\pi)}{c^2 r^2_{f,uv(i)}(t_f)}\mathbf{R}_2^{-1}\begin{bmatrix} u_{f(i)}(t_f)\left\{1-J_2R_p^2\cos^2 B_s\dfrac{3v^2_{f(i)}(t_f)-u^2_{f(i)}(t_f)}{r^4_{f,uv(i)}(t_f)}\right\}\\ v_{f(i)}(t_f)\left\{1+J_2R_p^2\cos^2 B_s\dfrac{3u^2_{f(i)}(t_f)-v^2_{f(i)}(t_f)}{r^4_{f,uv(i)}(t_f)}\right\}\end{bmatrix}, \tag{37}$$

$$\begin{bmatrix} u_{f(i)}(t_f)\\ v_{f(i)}(t_f)\end{bmatrix}=\mathbf{R}_2\begin{bmatrix} f_{pf(i)}(t_f)\\ g_{pf(i)}(t_f)\end{bmatrix}. \tag{38}$$

The second loop is an iterative procedure to find a self-consistent solution of Eqs. (34)–(38). Once this is complete, we proceed with the primary loop. The next step is to update the value of $w_{f(i)}(t_f)$. We calculate it by assuming that the occulting feature lies in the equatorial plane of the planet. Then:

$$w_{f(i)}(t_f)=v_{f(i)}(t_f)\cot B_s. \tag{39}$$

Finally we test for convergence of our primary loop. To do this, we calculate the change in planet-plane radius since the previous iteration:

$$\varepsilon_{(i)}=|r_{f,uv(i)}(t_f)-r_{f,uv(i-1)}(t_f)|. \tag{40}$$

If $\varepsilon_{(i)}$ is not smaller than a specified value, we return to Eq. (31) and repeat the loop. On the other hand if the convergence criterion is satisfied, we make the assignments $u_f(t_f)=u_{f(i)}(t_f)$, $v_f(t_f)=v_{f(i)}(t_f)$, $w_f(t_f)=w_{f(i)}(t_f)$ and exit the loop here.

5.8 Feature Radius and Longitude

To find the orbital longitude of the point where the occulted starlight intercepted the ring feature, we first calculate $x(t_f)$, $y(t_f)$, and $z(t_f)$ with Eq. (25):

$$\mathbf{r}_{pf}|_{xyz}=\mathbf{R}_3\mathbf{r}_{pf}|_{uvw}. \tag{41}$$

Next we write an expression for the magnitude of the feature radius:

$$\begin{aligned} r_{pf}(t_f) &\equiv |\mathbf{r}_{pf}(t_f)| \\ &= \sqrt{x_f^2(t_f)+y_f^2(t_f)+z_f^2(t_f)}, \\ &= \sqrt{u_f^2(t_f)+v_f^2(t_f)+w_f^2(t_f)}. \end{aligned} \tag{42}$$

For the special case of rings that are not inclined relative to the planet's equatorial plane, this simplifies to

$$r_{pf}(t_f)=\sqrt{u_f^2(t_f)+v_f^2(t_f)\csc^2 B_s}. \tag{43}$$

The orbital longitude, $\theta(t_r)$, is the angle $x\rightarrow y$ in the equatorial plane of the planet. The zero point for orbital longitude is the ascending node of the intersection of the Earth's equatorial plane for J2000.0 with the planet's ring plane:

$$\begin{aligned} \sin\theta(t_f) &= y_f(t_f)/r_{pf}(t_f), \\ \cos\theta(t_f) &= x_f(t_f)/r_{pf}(t_f). \end{aligned} \tag{44}$$

The only approximations involved in deriving the final results expressed in Eqs. (42)–(44) are (i) omission of special relativity, (ii) our approximations for general relativistic bending, (iii) the linear approximation for the solar-system barycentric velocity of the planet, and (iv) the finite number of iterations used to calculate $u_f(t_f)$, $v_f(t_f)$, and $w_f(t_f)$.

5.9 Model Times and Radii

In order to fit feature times and radii to a model, we shall need a procedure for calculating a "model radius" and "model time" that corresponds to each observed feature radius, $r_{pf}(t_f)$, and feature occultation time, t_f. For circular features, the model radius, $r_m(t_f)$, is just the semi-major axis (radius) of the feature, a_f. The model time, however, is that time at which the star would have been occulted by a feature at the model radius, a_f, rather than the time t_f, when it was occulted by the "observed radius" of the feature, $r_{pf}(t_f)$. We represent the time derivative of the observed radius by $\dot{r}_{pf}(t_f)$. Then the model time, t_m, is given by the equation

$$t_m=t_f-\frac{r_{pf}(t_f)-a_f}{\dot{r}_{pf}(t_f)}. \tag{45}$$

6. NUMERICAL IMPLEMENTATION OF MODEL FITTING

Equally important with an explicit algebraic development of the ring-orbit geometry are specifications of the input parameters and the numerical procedures used to fit the model to the feature times. In this section we present the sources for the ephemerides and all other numerical input (summarized in Table 4); also we describe our numerical implementation of the algebra of the previous section into a least-squares fitting procedure. All the calculations to be described were implemented in *Mathematica* (Wolfram 1991). The "notebook" front end ran on various Macintosh computers, which were connected to a "kernel" on one of several UNIX workstations in order to increase the speed of computation. Although numerical calculations carried out with *Mathematica* are not as fast as the inherent speed of a given computer, its capability for symbolic manipulation and the extensive documentation provided by a notebook proved of great benefit in working with this complex model.

6.1 Calculating Model Times and Radii

For our *HST* ephemeris, we used the "definitive ephemerides" provided by the Flight Dynamics Facility at NASA's Goddard Space Flight Center; these are available through the *HST* Archives at Space Telescope Science Institute (Baum 1993). The ephemerides consist of binary files giving spacecraft coordinates (X_{er}, Y_{er}, Z_{er}) and velocity components in the J2000.0 frame. They are tabulated at approximate minute intervals.

In order to perform a joint fit of these data with those from the 28 Sgr event, we needed a method for including the coordinates of ground-based observers in our calculations. We converted observatory locations into geocentric "observer ephemerides," which is the form most easily used with the approach adopted here. We used the geodetic coordinates of each observatory provided in Table I of F93. These were converted to geocentric coordinates using the equatorial radius and flattening values for the Earth given in Table 4, then nutated and precessed to find J2000.0 coordinates versus time $[X_{er}(t), Y_{er}(t), Z_{er}(t)]$. The conversion used does not include geodetic datum offsets or altitude corrections because the values of these quantities were uncertain; nor does it include the small effects (up to 0.3 arcsec or 0.009 km at surface of Earth) of polar motion.

The Saturn and Earth ephemerides used in these analyses were generated for us by L. Wasserman from the JPL DE-130 (Standish 1990). They are solar-system barycentric, geometric ephemerides for the Saturn system barycenter and for the Earth center, which we converted from B1950.0 to J2000.0 with the matrix $\mathbf{X}(0)$ given by Eq. (5.711-4) in Standish *et al.* (1992). We chose this matrix from the various methods available in the literature for precession between these two epochs, because it reproduced the conversion of test points in the DE-130 ephemeris to the DE-202 ephemeris. The ephemerides, tabulated at 10 min intervals in TDB, supplied (X_b, Y_b, Z_b), (X_e, Y_e, Z_e) and their time derivatives. The ephemerides for eight Saturnian satellites (see Table 4) were supplied by the Navigation Ancillary Information Facility (NAIF) at the Jet Propulsion Laboratory (JPL) (Acton 1990).

The position of GSC 6323-01396 is given in Table 4 in FK4 J2000.0. For use in the geometric modeling, the star's position was converted from FK4 to FK5 (Green 1985).

TABLE 4. Parameters always fixed in model fits.

Parameter	Value	Reference
Physical Constants		
speed of light, c (km s^{-1})	299792.458	Seidelmann (1992)
Receiver Coordinates		
Ground-based observatories		Table I of F93
HST ephemeris	file "PBA20000R.ORX"	Space Telescope Science Institute
Earth and Moon		
Barycenter ephemeris	DE-130	Standish (1990)
Mass ratio, M_e/M_m	81.300587	DE-130 (Standish 1990)
Earth radius (km)	6378.137	MERIT 1983 (Archinal 1992)
Earth flattening	1/298.257	MERIT 1983 (Archinal 1992)
Saturn system		
Barycenter ephemeris	DE-130	Standish (1990)
Satellite ephemerides	file "SAT018H.BSP"	NAIF (Acton 1990)
$J_2R_p^2$ (km^2)	59316335.9433	Table VII of F93
GM_{system} (km^3 s^{-2})	37940626.075	(W. M. Owen, private communication)
GM_p (km^3 s^{-2})	37931246.375	derived from system and satellite masses
GM_{Mimas} (km^3 s^{-2})	2.5	(W. M. Owen, private communication)
$GM_{Enceladus}$ (km^3 s^{-2})	5.6	(W. M. Owen, private communication)
GM_{Tethys} (km^3 s^{-2})	44.1	(W. M. Owen, private communication)
GM_{Dione} (km^3 s^{-2})	77.3	(W. M. Owen, private communication)
GM_{Rhea} (km^3 s^{-2})	154.1	(W. M. Owen, private communication)
GM_{Titan} (km^3 s^{-2})	8977.7	(W. M. Owen, private communication)
$GM_{Hyperion}$ (km^3 s^{-2})	1.	(W. M. Owen, private communication)
$GM_{Iapetus}$ (km^3 s^{-2})	117.4	(W. M. Owen, private communication)
Stars		
28 Sgr		
FK4/B1950.0	$\alpha_{s'}$ = 18^h 43^m 19^s.7946475	F93
	$\delta_{s'}$ = −22° 26' 46".88424	
FK5/J2000.0	$\alpha_{s'}$ = 18^h 46^m 20^s.5958671	derived from the B1950.0 position
	$\delta_{s'}$ = −22° 23' 32".0525118	
proper motion	0	approximation for this reduction
parallax	0	approximation for this reduction
GSC6323-01396		
FK4/J2000.0	$\alpha_{s'}$ = 20^h 10^m 30^s.35	Bosh and McDonald (1992)
	$\delta_{s'}$ = −20° 36' 47".6	
FK5/J2000.0	$\alpha_{s'}$ = 20^h 10^m 30^s.4275	derived from the FK4 position
	$\delta_{s'}$ = −20° 36' 47".6	
proper motion	0	assumption
parallax	0	assumption
Transformations		
B1950.0->J2000.0	rotation with X(0)	Eq. (5.711-4) of Standish *et al.* (1992)
TDB -> UTC	function library "SPICELIB"	Acton (1990)
SOGS seconds -> MJD	programs "orx2eph" and "preph"	(J. W. Percival, private communication)
Precession of receiver	procedure on p. B18	USNO (1992)
Nutation of receiver	procedure on p. B20	USNO (1992)
geodetic->geocentric	Eq. (4.22-7)	Archinal (1992)

The B1950.0 astrographic position of 28 Sgr is given in F93, and is reproduced in Table 4. In addition, the J2000.0 position of 28 Sgr is given.

We chose Modified Julian Date (MJD) as our reference time scale. In order to convert the times in the Saturn ephemeris from TDB to MJD, we first converted to UTC using a routine provided by the NAIF (Acton 1990). The time scale for the occultation light curve was derived from the spacecraft clock, described by keywords in the data file header. In the early stages of these analyses, we found that the data descriptor keywords were not accurate. The "EXPSTRT" keyword contained the value for the *predicted* start time, not the actual start time. In our case, these differed by about 24.5 s. In more recent data files, the keywords have been corrected, and the "EXPSTART" (note the addition of an "A") keyword value correctly describes the UTC as calculated using the database calibration for the spacecraft clock.

Another class of numerical input needed to calculate model times and radii consists of those parameters that we shall ultimately determine through least-squares fitting: ring-plane pole position, feature radii, clock offsets, star position offsets, and planet ephemeris offsets. The initial values of these quantities were generally taken from F93. Following the convention of F93, we use UTC 1980 November 12 23:46:32 (MJD 44555.99065) as the epoch for the pole position when considering pole precession, but we express the coordinates of the pole in the equator and equinox of J2000.0.

The final numerical ingredient in our model calculation is the set of feature occultation times. For this work, we used only those features with presumed-circular orbits

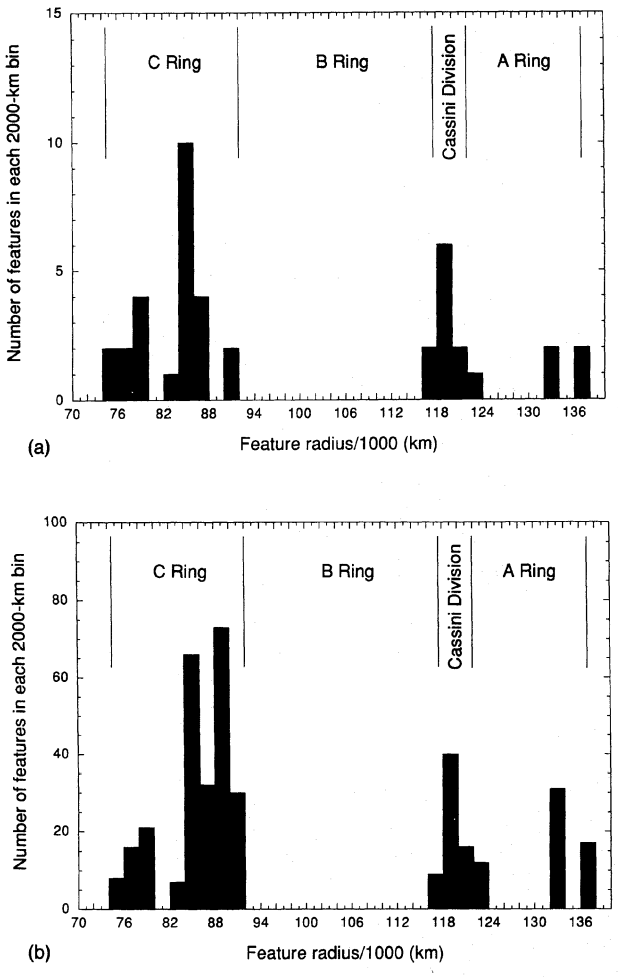

FIG. 12. Distribution of features with ring plane radius. Number of features in each 2000 km bin is plotted against feature radius for two analyses: (a) GSC 6323-01396 and (b) GSC 6323-01396 and 28 Sgr.

(F93), excluding B ring features as did F93. The measurements of the times for these features in the 28 Sgr data are described in F93 and Hu93. For the *HST* data, we measured the times of ring features in a manner consistent with the measurements of the Voyager and 28 Sgr data (see Sec. 4 above). This produced a total of 25 separate features measured in the *HST* data for use in the ring orbit fits. Fifteen of these occulted the star twice, for a total of 40 measurements of presumed-circular features. Five additional features are included in the 28 Sgr measurements, but were not crossed during the *HST* observations.

Figure 12 shows the distribution in ring-plane radius of the (a) GSC 6323-01396 features and (b) the combined GSC 6323-01396 and 28 Sgr features. These features span the area from the C ring to the outer A ring, with a gap in the B ring due to its high optical thickness. A total of 378 event-time measurements for 30 features were used in our geometric models that combined the 28 Sgr and *HST* data sets.

Since the speed of the model calculation proved to be an issue, the sky-plane calculation of feature radii is broken into two parts. In the first part, we calculate term #1 of Eq. (15), $\mathbf{r}_{\rm rp}(t_{\rm r},t_\pi)$ for each observed feature time. Since this part of the calculation has to be done only once, the results are then stored to a file for later use in fitting the model. In the second step, we read in this file and perform the fit. Splitting the calculation in this way introduces a small approximation because the value of $\mathbf{r}_{\rm rp}(t_{\rm r},t_\pi)$ depends on knowledge of the time t_π, which in turn depends on the star position. Therefore, if the star position is changed later in the calculation (when fitting for a star position offset), this previous determination of t_π is no longer exact.

Because the value of $\mathbf{r}_{\rm rp}(t_{\rm r},t_\pi)$ is calculated at the specific time $t_{\rm r}$, any change in this observed time when finding the model time requires a change in the value of the quantity. To calculate the values of time-variable quantities, we began by using a Taylor series to second order. We found no significant difference between second- and first-order series, so the first-order series was used thereafter.

As noted above, there are two iteration loops in the model: one for $w_{{\rm f}(i)}(t_{\rm f})$, the component of the feature vector in the direction of the star, and one to determine the magnitude of bending due to general relativity. For both of these iteration loops, the convergence criterion was a change in the quantity of less than 0.25 km.

6.2 Fitting the Model

For modeling the geometry of this occultation, we used standard nonlinear least-squares fitting techniques (Press *et al.* 1988). Our procedure employs numerical derivatives, and model parameters can be free to vary or held fixed for a given fitting sequence. The model fits are iterated until the change in all fitted parameters is well below 0.001 of their formal error. Our code allows minimizing the sum of squared residuals either in time or radius. For the 28 Sgr data, it makes little difference whether the fit is done in time or radius, since the apparent stellar track through the ring system is nearly linear, so that most time and radius residuals are proportional to each other. However, for the looping path of the *HST* occultation (Fig. 4), time and radius residuals are not proportional for cases where the apparent path of the star approaches tangency to the features. Hence, fits in time and radius can produce significantly different fitted parameters.

If the errors in the feature times followed a Gaussian distribution, then minimizing the sum of squared time residuals would be the correct procedure. However, if the feature times have other types of errors (such as noncircular orbits for some features), then fitting in radius might be more appropriate. Hence we have tried both approaches. For the fits in radius, we calculate the "observed radius" from the feature time and all other input parameters, following the procedure described in Sec. 5 that culminates with Eq. (42). The model radius for circular features is just its semimajor axis, a, as described earlier. For fits in time, the observed time is $t_{\rm f}$, and the model time is $t_{\rm m}$, given by Eq. (45).

TABLE 5. Sample values of ephemerides.

TDB	Position (km)			Velocity (km s^{-1})		
Solar System Barycenter –> Earth Center						
	X_e	Y_e	Z_e	$\dot{X}_e$	$\dot{Y}_e$	$\dot{Z}_e$
1991 10 3 0 0 0	148008535.410	22715784.937	9836798.495	–5.339123	26.875007	11.653409
1991 10 3 5 0 0	147911481.540	23199394.582	10046498.750	–5.444636	26.859338	11.646592
1991 10 3 10 0 0	147812528.660	23682718.898	10256074.851	–5.550124	26.843303	11.639614
1991 10 3 15 0 0	147711677.251	24165751.301	10465523.891	–5.655583	26.826903	11.632474
Earth Center –> HST						
	X_{er}	Y_{er}	Z_{er}	$\dot{X}_{er}$	$\dot{Y}_{er}$	$\dot{Z}_{er}$
1991 10 3 0 0 0	–6050.361	2351.855	2543.274	–1.744000	–6.991000	2.314000
1991 10 3 5 0 0	–5770.992	–2077.364	3317.219	2.593195	–7.106929	0.068888
1991 10 3 10 0 0	–3127.246	–5657.543	2623.740	5.845894	–4.261192	–2.203911
1991 10 3 15 0 0	786.067	–6893.357	769.570	6.689000	0.366000	–3.502000
Solar System Barycenter –> Saturn System Barycenter						
	X_b	Y_b	Z_b	$\dot{X}_b$	$\dot{Y}_b$	$\dot{Z}_b$
1991 10 3 0 0 0	868965562.251	–1103544951.016	–493136507.485	7.319746	5.307125	1.877008
1991 10 3 5 0 0	869097312.007	–1103449415.572	–493102718.130	7.319116	5.307924	1.877365
1991 10 3 10 0 0	869229050.434	–1103353865.738	–493068922.346	7.318487	5.308724	1.877722
1991 10 3 15 0 0	869360777.533	–1103258301.517	–493035120.132	7.317857	5.309523	1.878079
Saturn System Barycenter –> Saturn Center						
	X_{bp}	Y_{bp}	Z_{bp}	$\dot{X}_{bp}$	$\dot{Y}_{bp}$	$\dot{Z}_{bp}$
1991 10 3 0 0 0	293.330	–72.329	–19.548	0.000327	0.001239	–0.000111
1991 10 3 5 0 0	298.348	–49.723	–21.482	0.000228	0.001272	–0.000104
1991 10 3 10 0 0	301.504	–26.601	–23.288	0.000121	0.001295	–0.000096
1991 10 3 15 0 0	302.669	–3.174	–24.943	0.000008	0.001305	–0.000087

6.3 Numerical Tests

We performed extensive numerical calculations to establish that our procedures yield the same numerical results as those used by F93. The first test was to check the numerical values of input ephemerides and to reproduce the numerical results described by F93, as in their Tables B-I and B-II. Since our respective calculations are carried out somewhat differently, some of the intermediate results could not be compared. We did compare ephemeris values (positions and velocities of Earth, Saturn barycenter, and barycenter offset due to satellites), observer positions, backdated time at feature crossing, magnitude of general relativity bending, ring radius and longitude. The agreement was usually within 0.003 km, with no discrepancies greater than 0.014 km. To facilitate tests of future analyses of these *HST* data, we have provided some check points for the *HST* and other ephemerides in Table 5 and a breakdown of our sky-plane calculations in Table 6.

The next numerical test was to fit the portion of the 28 Sgr data set used by F93. We fixed ring radii and clock offsets at the F93 values (note that our "offset time," t_o, to be subtracted from the recorded clock time, is the negative of the "station time offsets," to be added to the recorded clock time, used by F93). Then we fit for pole right ascension and declination and the ephemeris offsets. When we do this fit with B1950.0 ephemerides, our results agree with those of Fit 5 in Table VIII of F93 within 0°.0003 (0.006 of the formal error). We perform the same fit with J2000.0 ephemerides (Fit 1 in Table 7). Comparing this pole position with that obtained with the B1950.0 ephemerides and then converted to J2000.0 using the matrix procedure given in Table 4, we find agreement within 0°.0003 (0.007 of the formal error). Throughout our tests, we have found that the precession method we have adopted gives consistent results, independent of calculation epoch.

7. MODEL FITS TO THE OCCULTATION TIMES

Following the tests described in the previous section, we performed three types of fits: (i) fits to the 28 Sgr data, to determine the sensitivity of the solution to different assumptions than used by F93; (ii) fits with only the *HST* GSC 6323-01396 data set, to determine the overall usefulness of a single *HST* data set; and (iii) joint fits of the HST GSC 6323-01396 and the 28 Sgr data, to establish the pole position and radius scale for Saturn's rings independent from Voyager data. The fit results we present here were chosen to summarize what we learned from a much larger number of fits that were carried out.

7.1 A Further Test of the 28 Sgr Data

As noted by F93, model fits with only the 28 Sgr data yield a pole position that differs by several formal errors from the pole position determined by fits to both the 28 Sgr and Voyager data (see Fig. 13). Although the pole position adopted by F93 yields a feature radius scale that agrees with radii of bending waves determined from dynamical considerations, the failure of the 28 Sgr data set to stand on its own leads one to be suspicious of how this data set might be influencing the joint solution with Voyager. We note that the time residuals for their adopted solution given in Fig. 14 of F93 show a bimodal distribution for Palomar, systematically negative residuals for McDonald, and systematically positive residuals for the IRTF. This solution

TABLE 6. Numerical values for certain cases.

Quantity	Symbol	28 Sgr, MCD Test Case	GSC6323-01396, HST Test Case
Pole position[a], J2000 (deg)	α_n, δ_n	40.587582 83.534223	40.586206 83.534078
Star position, J2000 (deg)	$\alpha_{s'}, \delta_{s'}$	281.5858161129 −22.3922368088	302.6267812500 −20.6132222222
Planet ephemeris offset (km)	f_o, g_o	0.0 0.0	0.0 0.0
Star position offset (arcsec)	α_o, δ_o	0.164221 −0.125531	0.956999 −0.107345
Clock offset (s)	t_o	−0.077274	0.0
Feature name		38	23
Clock time (UTC)	t_c	1989 7 3 8 41 12.4041	1991 10 3 2 2 21.5950
Received time (UTC)	t_r	1989 7 3 8 41 12.4814	1991 10 3 2 2 21.5950
Earth center (km)	$\mathbf{r}_e(t_r)\|_{fgh}$	2135192.637357 −1477916.428756 151969338.341209	136973906.170086 30580115.083202 53116337.204003
Receiver relative to earth center (km)	$\mathbf{r}_{er}(t_r)\|_{fgh}$	2420.217832 4872.313198 3322.601021	−4422.527537 3504.074565 4106.602768
Time at planet plane (UTC)	t_π	1989 7 3 7 26 10.7821	1991 10 3 0 42 55.2547
Planet system barycenter (km)	$\mathbf{r}_b(t_\pi)\|_{fgh}$	2061844.806959 −1475252.842513 1501525132.692888	136880668.806791 30586930.561072 1482033121.315271
Planet center relative to system barycenter (km)	$\mathbf{r}_{bp}(t_\pi)\|_{fgh}$	−222.297581 −52.003695 −155.623141	210.465321 57.771464 209.921215
Velocity of planet center relative to solar system barycenter (km s^{-1})	$\dot{\mathbf{r}}_p(t_\pi)\|_{fgh}$	9.142927 0.345519 −0.085487	9.027025 1.572242 −1.151416
Planet center relative to receiver (km)	$\mathbf{r}_{rp}(t_r, t_\pi)\|_{fgh}$	−75990.345811 −2260.730651 1349552316.127516	−88604.370437 3369.174768 1428912887.429715
Time at feature (UTC)	t_f	1989 7 3 7 26 10.7081	1991 10 3 0 42 55.1927
Light travel correction, feature to planet plane (km)	$\mathbf{r}_{pp}(t_f, t_\pi)\|_{fgh}$	0.676636 0.025571 −0.006327	0.559325 0.097418 −0.071343
Feature coordinates in shadow plane (km)	$f_f(t_r), g_f(t_r)$	75991.022447 2260.756221	88604.929762 −3369.077350
Shadow plane radius (km)	$\sqrt{f_f^2 + g_f^2}$	76024.644105	88668.958832
Magnitude of GR bending (km)	$f_s(t_\pi), g_s(t_\pi)$	30.181259 0.966742	27.353449 −1.010997
Feature coordinates at planet plane (km)	$\mathbf{r}_{pf}(t_f)\|_{uvw}$	75321.383569 10536.981586 22186.586431	88397.968737 7268.992081 18575.480601
Planet plane radius (km)	$\sqrt{u_f^2 + v_f^2}$	76054.840764	88696.330942
Feature coordinates in ring plane (km)	$\mathbf{r}_{pf}(t_f)\|_{xyz}$	−55552.810853 −56484.233442 0.000000	−28317.191257 −86082.659587 0.000000
Ring plane radius (km)	$\lvert\mathbf{r}_{pf}(t_f)\rvert$	79224.891424	90620.569421
Feature longitude (deg)	$\theta_{pf}(t_f)$	225.476318830	251.791199062

Notes to TABLE 6

[a] The pole position is the adopted solution, Fit 11 of Table 7. The predicted amount of pole precession has been added to the adopted solution value to get the value listed here.

was generated under the assumption that the time offsets (t_o) are zero for Cerro Tololo, McDonald, Palomar, the IRTF, and UKIRT. As a test of this assumption we performed Fit 2, which is identical to Fit 1 except that the time offsets for all stations except for the IRTF were free parameters. We chose the IRTF as a time reference because we are most familiar with its calibration (Ha93).

The results show a similar pole position to that of Fit 1, but the fitted parameter errors are larger. As shown in Table 8, the time offsets for two of the stations that F93 fixed at zero, McDonald and UKIRT, differ from zero by several formal errors. Also, most of the time offsets are negative, which could mean that the IRTF time scale and/or position is in error. We conclude from this exercise that significant inconsistencies remain in the 28 Sgr data set—possibly in the time scales and/or observatory coordinates used by F93 and in this work. We believe that these lingering systematic errors cause the 28 Sgr data set, when

TABLE 7. Results of orbit model fits.

Fit Code[a]	Data Incl. HST	Data Incl. 28 Sgr	Coordinates of Pole (deg, J2000) α_n	Coordinates of Pole (deg, J2000) δ_n	Epoch of Pole[b]	Precession Rate Ratio[c]	Radius of Feature 23 (km)	t_0 (HST) (s)	RMS	Radii
28 Sgr Data										
1	–	y	40.4444 ± 0.0470	83.6140 ± 0.0236	28 Sgr	0	90557.255 ± 17.695	–	1.272 km	free
2	–	y	40.3686 ± 0.1051	83.6289 ± 0.0279	28 Sgr	0	90551.879 ± 18.101	–	1.189 km	free
GSC6323-01396 Data										
3	y	–	40.5954 ± 0.0222	83.5374 ± 0.0051	HST	0	90615.027	0.06 ± 0.25	0.423 s	fixed
4	y	–	40.5837 ± 0.0299	83.5390 ± 0.0064	HST	0	90615.027	0.11 ± 0.23	2.366 km	fixed
5	y	–	40.5838 ± 0.0296	83.5434 ± 0.0064	HST	0	90615.027	–0.08 ± 0.26	2.337 km	fixed
6	y	–	40.5870 ± 0.0286	83.5381 ± 0.0061	HST	0	90615.027	0	2.338 km	fixed
7	y	–	40.6260 ± 0.4780	83.5266 ± 0.0521	HST	0	90609.935 ± 566.176	0	1.682 km	free
8	y	–	40.5955	83.5381	Voyager 1	1.4 ± 1.3	90614.87	0	2.170 km	fixed
GSC6323-01396 and 28 Sgr Data										
9	y	y	40.5841 ± 0.0154	83.5373 ± 0.0021	28 Sgr–HST	0	90615.027	0	1.791 km	fixed
10	y	y	40.5854 ± 0.0151	83.5340 ± 0.0053	28 Sgr–HST	0	90619.038 ± 4.607	0	1.328 km	free
11[d]	**y**	**y**	**40.5929 ± 0.0151**	**83.5348 ± 0.0053**	**Voyager 1**	**1**	**90618.526 ± 4.606**	**0**	**1.328 km**	**free**
Robustness Tests of Adopted Solution (Fit 11)										
12	y	y	40.6086 ± 0.0051	83.5266 ± 0.0031	Voyager 1	1	90625.356 ± 3.060	0	0.099 s	free
13	y	y	40.5869 ± 0.0151	83.5344 ± 0.0053	Voyager 1	1	90619.653 ± 4.597	0	1.329 km	free
14	y	y	40.5974 ± 0.0154	83.5372 ± 0.0056	Voyager 1	1	90615.559 ± 5.043	–0.24 ± 0.17	1.326 km	free

Notes to TABLE 7

[a] Fits were performed either in radius or in time. To distinguish between the two types, see the "RMS" column. Fit in radius will list the RMS in kilometers, fits in time will list it in seconds. Only Fits #3 and #12 are performed in time.

[b] The epoch "28 Sgr" is defined as the mean epoch of the 28 Sgr occultation, approximately 1989 Jul. 3 8:0:0. The epoch "HST" is the mean epoch of the occultation of GSC6323-01396, approximately 1991 Oct. 3 7:0:0. An entry of "28 Sgr–HST" indicates a mean epoch between these two mean epochs. The epoch "Voyager 1" is defined as UTC 1980 Nov. 12 23:46:32.

[c] The precession rate ratio is defined as the ratio of fitted to predicted precession rates. The predicted precession rates are those given by F93.

[d] Adopted solution

used by itself, to yield a pole position inconsistent (within its formal errors) with that adopted by F93.

7.2 Models with only GSC 6323-01396 Data

The first fits performed with *HST* data alone had feature radii fixed at the revised Voyager values (from Fit 9, Table VIII of F93; radii supplied by R. French), but with the pole coordinates and a possible offset to the *HST* clock allowed to vary. The results are presented in Table 7, with Fit 3 carried out in time and Fit 4 in radius. The right ascensions of the pole agree within 0.5 formal errors, and the declinations agree within 0.3 formal errors, so the choice between fitting in radius and time is significant, but not critical. We note that the rms residual in the time fit, 0.423 s, is substantially larger than the errors that have been estimated for the feature times ($\leqslant$0.1 s for 28 Sgr data and $\leqslant$0.2 s for *HST* data). This indicates an inadequate model, possibly due to yet undetected noncircularities in some of the features (not surprising at this early stage for

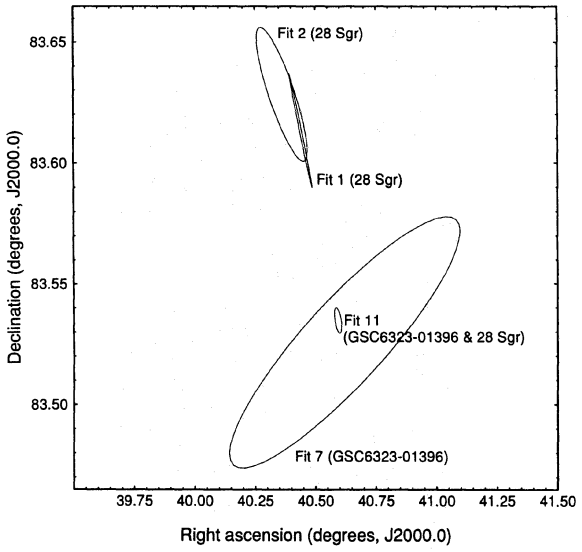

FIG. 13. Pole positions from fits using data from the occultation of 28 Sgr (Fits 1 and 2), data from the occultation of GSC 6323-01396 (Fit 7), and data from both occultations (Fit 11). All poles are plotted at the Voyager 1 epoch of 1980 November 12 23:46:32 UTC. Because Fits 1 and 2 were performed without pole precession and are therefore at the 28 Sgr epoch, the precession rate of F93 was added to the pole values for inclusion on this plot.

TABLE 8. Clock offsets for Fit 2 (28 Sgr).

Station Code[a]	Clock Offset, t_0 (s)	F93 Clock Offset[b], (s)
CAT	–0.064 ± 0.024	–0.030 ± 0.016
CTIO	–0.158 ± 0.158	0
ESO1	0.070 ± 0.155	0.219 ± 0.014
ESO2	0.053 ± 0.154	0.204 ± 0.015
IRTF	0	0
KPi	–0.103 ± 0.025	–0.064 ± 0.017
KPe	–0.079 ± 0.027	–0.059 ± 0.021
MCD	–0.067 ± 0.016	0
MMT	–0.096 ± 0.024	–0.068 ± 0.017
PAL	–0.016 ± 0.024	0
SPM	–0.005 ± 0.021	0.024 ± 0.011
UKIRT	–0.047 ± 0.016	0

Notes to TABLE 8

[a] Station naming conventions are after Table I of F93.

[b] F93 clock offset values have been reversed in sign to agree with our sign convention.

modeling Saturn ring orbits at this high precision). Hence we feel that the fits in radius would yield results closer to reality, so we shall carry out the remaining fits in radius.

Fit 5 of Table 7 is identical to Fit 4, except that the relative error between the planetary ephemeris and the star position has been expressed as an offset in km to the ephemeris (f_0 and g_0) rather than an offset in angle to the star position (α_0 and δ_0). Again, the differences between the right ascension and declination of the pole given by Fits 4 and 5 are not great. Faced with making the choice, however, we feel that the large offset of 1 arcsec would be more likely in the GSC position of the star, so we choose to relegate the offset to the star position in further fits.

Next we investigate the possibility of an offset to the *HST* clock. Since Fits 3–5 give clock offsets consistent with 0.0 s, we fix this parameter at 0.0 s for the remaining fits. Fit 6 shows that the result does not change significantly when the time is thus fixed.

In Fit 7, we allow all feature radii and pole coordinates to be free parameters. With this many free parameters, the formal errors are significantly larger, but we do get a result that agrees with previous work within the formal errors. The final fit presented with only *HST* data (Fit 8) is a fit in which the radii and pole parameters were fixed at F93 final values. The fit was then performed for the precession rate, expressed as a ratio of the fitted value to the value calculated by F93. Their calculation includes solar torque on Saturn, and the torque transmitted to Saturn through its satellites (principally Titan). For this fit, we find a ratio 1.4 ± 1.3, a value consistent with their calculated rate, but with an uncertainty too large to draw any conclusions about the precession of Saturn's ring-plane pole.

7.3 Models Combining GSC 6323-01396 and 28 Sgr Data

In Fits 9, 10, and 11 we used both the *HST* and 28 Sgr data sets. In Fit 9, ring radii were fixed at the revised Voyager values. In Fit 10, the radii were free parameters. The rms residual of the fit is substantially less, but the change in the pole position is well within the errors. Fit 11 includes all station time offsets (except *HST* and IRTF) as free parameters. Again the rms residual decreases, but the pole coordinates do not change. The results of these fits are listed in Table 7 and also plotted in Figs. 13 and 15. We determined that the 27 month time interval between the 28 Sgr and the GSC 6323-01396 occultations was not long enough to establish the precession rates from these data.

7.4 Adopted Solution

Fit 11 gleans the most information from the combination of the *HST* and 28 Sgr data sets without incorporating Voyager data, so we have adopted it as our best solution. The parameters and their formal errors for our adopted solution are given in Table 9. Radius residuals are shown in Fig. 14.

We now check the sensitivity of our adopted solution to those procedures that are a matter of judgment, as discussed above. We have performed fits that each have one of these procedures reversed from our adopted solution: Fit 12 has been done in time instead of radius, Fit 13 has f_0 and g_0 instead of α_0 and δ_0 as free parameters to describe the offset between the planet ephemeris and the star position, and Fit 14 allows the *HST* clock to have an offset. The coordinates for the pole in Fit 12 differ from that of our adopted solution by 1–1.5 formal errors of the adopted solution, but in other cases the differences are smaller. We note that for Fit 14, which has the time offset for the *HST* as a free parameter, the fitted *HST* time offset differs from zero by 1.4 formal errors. This could well have been forced by the remaining uncertainties in clock offsets and observatory coordinates for the 28 Sgr data set discussed above.

The reliability of our adopted solution depends not only on the formal errors and suitability of the procedures just discussed, but also on the accuracy of the assumptions on which our analysis has been based. Most of these potential systematic errors have been discussed by F93, and their conclusions concerning errors in observatory positions, ring plane distortions, and general relativity would apply here as well. They also bring up the issue of the direction to the occulted star changing during the occultation—due to the effects of proper motion and parallax—and they show that these effects can be neglected for 28 Sgr. Because the data-recording interval for the occultation of GSC 6323-01396 was about five times as long as that for 28 Sgr, however, we need to reexamine the parallax and proper motion issue. Since these quantities are not presently known for GSC 6323-01396, we cannot determine the changing direction explicitly. We do note that the star is about 6 mag fainter than 28 Sgr, meaning that it should be about ten times more distant, which would give it a parallax about ten times less. Furthermore, the length of the chord for the GSC 6323-01396 occultation is less than half that for 28 Sgr, and the former occultation occurred well away from opposition. Both of these effects would further reduce the change in the direction of the star due to parallax. Though we feel that it is unlikely that the effects of proper motion and parallax would be large enough to be

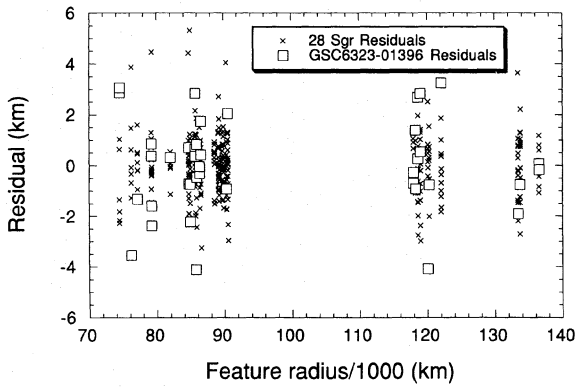

FIG. 14. Radius residuals for the adopted fit, Fit 11 in Table 7. Residuals for the GSC 6323-01396 data set are plotted as open squares, while those from the 28 Sgr data sets are plotted as crosses. All 28 Sgr data sets are included and have been plotted with the same symbol.

TABLE 9. Adopted solution.[a]

Saturn Pole, Voyager 1 epoch	Adopted Solution, present work	Difference[b]
α_n (deg, J2000.0)	40.5929 ± 0.0151	−0.0026
δ_n, (deg, J2000.0)	83.5348 ± 0.0053	−0.0036
$d\alpha_n/dt$ (deg yr^{-1}, J2000.0)	−0.00061172	0.000
$d\delta_n/dt$ (deg yr^{-1}, J2000.0)	−0.00006420	0.000

Stellar-position offsets	28 Sgr	GSC6323-01396
$\alpha_o \cos \delta_s$ (arcsec)	0.1518 ± 0.0004	0.8957 ± 0.0005
δ_o (arcsec)	−0.1255 ± 0.0005	−0.1073 ± 0.0006

Station Code[c]	Clock Offset, t_o (s)	Difference[b] (s)	RMS (km)
HST	0.		1.85
CAT	−0.080 ± 0.019	−0.500	1.27
CTIO	−0.080 ± 0.035	−0.080	0.77
ESO1	0.146 ± 0.035	−0.073	1.23
ESO2	0.129 ± 0.035	−0.075	1.50
IRTF	0.	0.000	1.04
KPi	−0.119 ± 0.021	−0.055	1.50
KPe	−0.100 ± 0.023	−0.041	0.72
MCD	−0.077 ± 0.013	−0.077	0.83
MMT	−0.112 ± 0.020	−0.044	1.53
PAL	−0.038 ± 0.014	−0.038	0.95
SPM	−0.023 ± 0.015	−0.047	1.29
UKIRT	−0.037 ± 0.017	−0.037	1.84

Feature[c]	Semimajor Axis (km)	Difference[b] (km)	RMS (km)	Feature[c]	Semimajor Axis (km)	Difference[b] (km)	RMS (km)
44	74495.21 ± 4.17	4.45	2.06	41	89298.49 ± 4.57	3.43	1.11
40	76266.98 ± 4.17	3.05	2.01	26	89790.11 ± 4.59	3.31	0.73
39	77167.80 ± 4.20	3.17	0.85	25	89942.85 ± 4.59	3.57	0.86
38	79223.59 ± 4.24	3.28	0.82	24	90407.26 ± 4.60	3.18	1.55
37	79268.12 ± 4.25	2.84	1.78	23	90618.53 ± 4.61	3.66	1.25
36	82043.80 ± 4.32	3.22	0.51	20	117936.60 ± 5.71	4.35	0.66
35	84752.66 ± 4.38	3.22	1.36	16	118287.69 ± 5.72	4.40	0.80
34	84952.54 ± 4.39	3.16	1.64	13	118632.67 ± 5.73	4.56	1.40
33	85663.96 ± 4.40	3.31	0.67	15	118970.06 ± 5.75	4.37	1.46
42	85761.82 ± 4.41	3.23	1.67	12	120076.54 ± 5.81	3.12	1.75
31	85924.14 ± 4.41	2.76	1.30	11	120251.12 ± 5.82	4.81	1.02
30	86373.75 ± 4.43	3.14	0.73	7	122054.05 ± 5.89	4.57	1.43
29	86604.45 ± 4.44	3.34	1.07	4	133428.39 ± 6.37	4.86	1.38
28	88597.76 ± 4.55	3.47	0.88	3	133750.06 ± 6.39	4.92	1.28
27	89191.82 ± 4.57	3.22	0.74	1	136527.40 ± 6.52	5.12	0.53

Notes to TABLE 9

[a] Fit 11 of Table 7.
[b] Tabulated differences are values of this work minus those of F93.
[c] Station and feature naming conventions are after F93.

significant, we must await measurements of these quantities before we can be sure.

Errors in the *HST* ephemeris would directly propagate into our solution for the ring geometry, but one would expect that it would be easier to maintain an ephemeris for an Earth-orbiting spacecraft, rather than one so distant as Voyager during its Saturn encounter. The stated accuracy of the *HST* ephemeris is 0.2 km (Elkin 1990). Referred to an Earth-based observer, the *HST* ephemeris errors can be described by three components: "in-track" (along the instantaneous direction of motion, as seen by the observer), "range" (along the line of sight from the observer to the *HST*), and "cross-track" (orthogonal to the other two directions). Using plates taken at Anderson Mesa of the Lowell Observatory, Slivan (1991) found the cross-track position of the *HST* to be within 0.05 km of the definitive ephemeris values, but due to the difficulty in defining the time of the plate exposure to better than 1.0 s, the in-track uncertainty of the result was several kilometers. The range error was unobservable. Another check we have on the *HST* ephemeris is that an in-track error would appear as an error in the *HST* clock. When fit as a free parameter, the zero point moves to 0.1 ± 0.2 s—equivalent to a 0.8 ± 1.6 km in-track error.

Another factor to consider is the weighting of the timings used for the fits. We have tried no schemes other than equal weighting. For light curves with ideal Gaussian noise, we should be weighting each feature time inversely proportionally to the square of its rms error. We have not attempted this because we do not believe that our light curves have only ideal Gaussian noise. One way to see what effect a different weighting scheme would have on the

results is to compare our fits in time to those in radius (Fits 12 and 11). We prefer fitting in radius for the reasons discussed earlier, but fitting in time effectively gives a higher weight to measurements in those sections of the *HST* light curve for which the apparent radial velocity of the star is low. This different weighting alters the results, but not drastically.

7.5 Comparison with Other Solutions

Now we can compare the results of recent determinations of Saturn's ring-plane pole, based on models that include the feature radii as well as the pole coordinates as free parameters. These solutions are based on three data sets: Voyager (which includes both the PPS and RSS occultation data), 28 Sgr, and *HST*. Plots of the pole solutions from Earth-based data are shown in Fig. 13, where we see the results from four solutions, each having the pole and radii free: 28 Sgr alone (under two different assumptions about the observatory time offsets), *HST* alone, and our adopted solution for the combined *HST* and 28 Sgr data sets. In Figs. 15(a) and 15(b), which have greatly expanded scales compared with that of Fig. 13, we have plotted the poles and their error ellipses for various combinations of data from Voyager, 28 Sgr, and GSC 6323-01396. Figure 15(a) shows pole solutions with feature radii fixed, and Fig. 15(b) shows solutions with feature radii as free parameters. The solution using only Earth-based data is consistent with that for Voyager, although with larger formal uncertainties. The solutions involving Voyager data have smaller formal uncertainties than the Earth-based solution due to the different aspects probed by the two Voyager occultations. However, we emphasize that cross-track trajectory errors and pole precession were fixed parameters in both the NCP and F93 solutions, so the actual uncertainties in those pole positions may be somewhat larger.

Differences between our adopted solution and that adopted by F93 for all fitted parameters are given in Table 9. Our independent result confirms the general placement of the pole given by NCP and F93. Independent tests of the radius scale come from the density waves (Brophy & Rosen 1992) and Pan wakes (Showalter 1991), as discussed by F93.

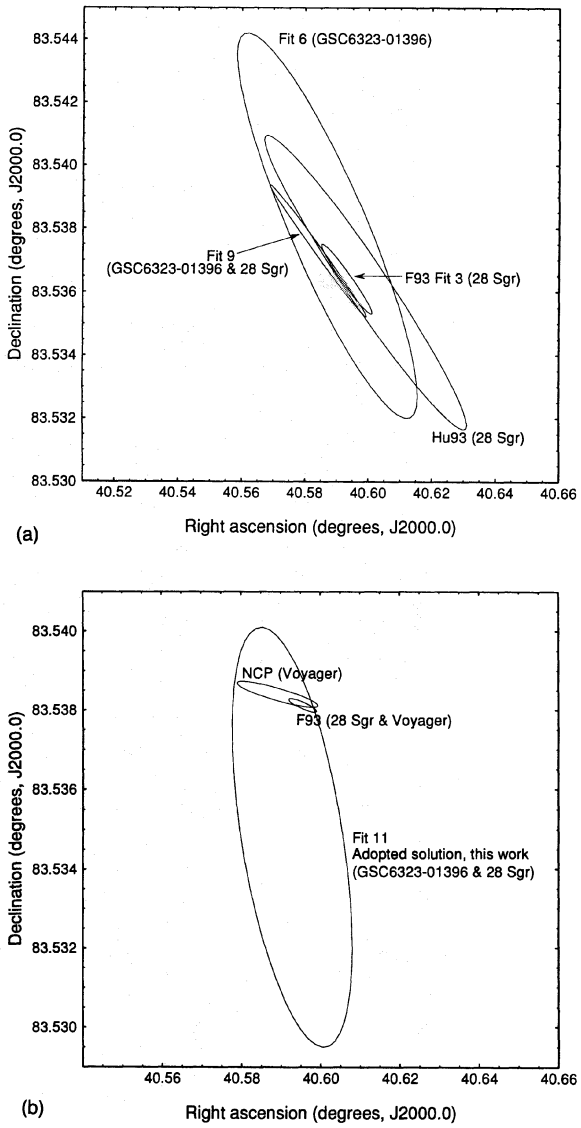

FIG. 15. Pole positions for fits described in text. (a) The pole positions from fits in which feature radii are fixed parameters. These include fits with data from only GSC 6323-01396 (Fit 6), data from GSC 6323-01396 combined with data from 28 Sgr (Fit 9), as well as a fit with 28 Sgr data from F93 (F93 Fit 3), and the final result from Hu93. Note that while Fits 6, 9, and F93 Fit 3 all held radii fixed at the revised NCP values (Fit 9 of Table VIII in F93), Hu93 fixed radii at the values originally published by NCP. See F93 and Hu93 for details. (b) The adopted solution from this work (Fit 11) is plotted with the solutions of NCP and F93, all of which allowed feature radii to be free parameters.

8. CONCLUSIONS

A significant result of this work is the demonstration that a single Earth-orbiting observatory can produce data that are calibrated well enough in space and time to allow a simultaneous solution for the radius scale and pole of Saturn's rings. Contrary to observations with multiple ground-based stations, these data were recorded relative to a single time base and observatory ephemeris. Data of this photometric quality for a star of this magnitude cannot be obtained from the ground with present techniques at optical or IR wavelengths.

Systematic errors still remain in the 28 Sgr data. From our tests it appears that these may result from errors in the observatory positions, which should be remeasured on a common system. Until these errors are corrected, we must remain cautious in estimating the true accuracy of models involving this data set.

This work, along with F93 and Hu93, begins the incorporation of Earth-based occultation data into a global kinematic model of Saturn's rings. The next step in this enterprise will be to improve upon current solutions by combining the *HST*, Voyager, and 28 Sgr data sets. The freely precessing, noncircular features can be added to the

kinematic model, allowing Saturn's gravitational harmonics to be fitted as free parameters. In addition to possibly revealing new noncircular features, this work will improve the ring-system fiducial available for the Cassini mission. To measure the precession of the rings and the ring-plane pole, we shall need to continually acquire data. With the imminent demise of the HSP, the challenge will be to find occultation events that would yield adequate signal to noise with the FOS or with ground-based instruments (most likely in the IR).

We are encouraged about the potential of Earth-orbital observations of stellar occultations. The main improvement for a future spacecraft would be to minimize the restrictions on the times when data can be acquired. A higher orbit would allow more continuous data recording, with fewer interruptions (which prohibited recording of two-thirds of our potential light curve) for Earth occultation and SAA passages. Reductions in the solar and lunar avoidance zones would also increase the observational opportunities. Further advantage could be gained with extremely large orbits that would permit observation of occultations not visible from Earth. CCD's and IR array detectors would achieve greater signal to noise through their higher quantum efficiencies and their facility for more efficient background rejection.

Many people on the Space Telescope Project made essential contributions to the success of these observations. Specifically we thank P. Stanley for her heroic efforts in scheduling our SV test and these observations. A. Lubenow also had a critical role in scheduling this occultation. J. Younger implemented commanding changes shortly before the program was carried out, and R. White helped us to correct the offset acquisition commands. A. Storrs and P. Brodsky provided explanations of the management procedures used at the Space Telescope Science Institute for processing proposals and converting their instructions to spacecraft commands. S. McDonald measured the target positions; J. Kangas and S. Slivan wrote the software that we used to predict the occultation. We are grateful to R. French, P. Nicholson, W. Hubbard, and C. Porco for use of data in advance of publication. N. Donahue helped with the synthetic Saturn figures, and L. Young and C. Olkin critically reviewed a draft of Sec. 5. P. Nicholson and W. Hubbard (as referee) provided helpful comments on the manuscript. This work was supported, in part, by HSP GTO Grant No. NASG5-1613. A.S.B. is partially supported by the NASA Graduate Student Researcher Program, and M.L.C. is supported by a NASA Planetary Astronomy Postdoctoral Fellowship.

REFERENCES

Acton, Jr., C. H. 1990, in AIAA/NASA Second International Symposium on Space Information Systems, edited by L. A. Tavenner (AIAA, JPL, Pasadena, CA), Vol. 2, p. 1029
Alexander, A. F. O'D. 1962, Planet Saturn: A History of Observation, Theory, and Discovery (Macmillan, New York)
Archinal, B. A. 1992, in Explanatory Supplement to the Astronomical Almanac, edited by P. K. Seidelmann (University Science Books, Mill Valley, CA), p. 199
Baron, R. L., Dunham, E. W., & Elliot, J. L. 1983, PASP, 95, 925
Baum, S. 1993, HST Archive Manual (St Sci)
Bless, R. C., *et al.* 1994, in preparation
Bless, R. C., Percival, J. W., Walter, L. E., & White, R. L. 1992, Hubble Space Telescope High Speed Photometer Instrument Handbook (St Sci)
Boggess, A., *et al.* 1978a, Nature, 275, 377
Boggess, A., *et al.* 1978b, Nature, 275, 372
Bosh, A. S., & McDonald, S. W. 1992, AJ, 103, 983
Brophy, T. G., & Rosen, P. A. 1992, Icarus, 99, 448
Burrows, C. J., Holtzman, J. A., Faber, S. M., Bely, P. Y., Hasan, H., Lynds, C. R., & Schroeder, D. 1991, ApJ, 369, L21
Cuzzi, J. N., Lissauer, J. J., Esposito, L. W., Holberg, J. B., Marouf, E. A., Tyler, G. L., & Boischot, A. 1984, in Planetary Rings, edited by R. Greenberg and A. Brahic (University of Arizona Press, Tucson), p. 73
Downes, R. 1992, Hubble Space Telescope Phase II Proposal Instructions (St Sci)
Dunham, E., Elliot, J. L., Mink, D. J., & Klemola, A. R. 1982, AJ, 87, 1423
Dunham, E. W., Baron, R. L., Elliott, J. L., Vallerga, J. V., Doty, J. P., Doty, & Ricker, G. R. 1985, PASP, 97, 1196
Dunham, E. W., McDonald, S. W., & Elliot, J. L. 1991, AJ, 102, 1464
Elkin, D. 1990, private communication
Elliot, J., & Kerr, R. 1984, Rings: Discoveries from Galileo to Voyager (MIT, Cambridge)
Elliot, J. L. 1990, in Asteroids to Quasars, edited by P. Lugger (Cambridge University Press, New York), p. 27
Elliot, J. L., Dunham, E., & Mink, D. 1977, Nature, 267, 328
Elliot, J. L., Dunham, E., Wasserman, L. H., Millis, R. L., & Churms, J. 1978, AJ 83, 980
Elliot, J. L., Wasserman, L. H., Veverka, J., Sagan, C., & Liller, W. 1974, ApJ, 719
Elliot, J. L., Wasserman, L. H., Veverka, J., Sagan, C., & Liller, W. 1975, AJ, 80, 323
Esposito, L. W. 1986, Icarus, 67, 345
French, R. G., Elliot, J. L., & Allen, D. A. 1982, Nature, 298, 827
French, R. G., *et al.* 1988, Icarus, 73, 349
French, R. G., *et al.* 1993, Icarus, 103, 163
Green, R. M. 1985, Spherical Astronomy (Cambridge University Press, Cambridge)
Harrington, J., Cooke, M. L., Forrest, W. J., Pipher, J. L., Dunham, E. W., & Elliot, J. L. 1993, Icarus, 103, 235
Holberg, J. B., Nicholson, P. D., French, R. G., & Elliot, J. L. (1987), AJ, 94, 178
Hubbard, W. B., *et al.* 1993, Icarus, 103, 215
Keeler, J. E. 1889, AJ, 8, 175
Kinney, A. L. 1993, Faint Object Spectrograph Instrument Handbook (St Sci)
MacKenty, J. W., *et al.* 1992, Hubble Space Telescope Wide Field-Planetary Camera Instrument Handbook (St Sci)
Marouf, E. A., Tyler, G. L., Zebker, H. A., Simpson, R. A., & Eshleman, V. R. 1983, Icarus, 54, 189
Nicholson, P., Cooke, M. L., & Pelton, E. 1990, AJ, 100, 1339 (NCP)
Nicholson, P. D., Persson, S. E., Matthews, K., Goldreich, P. D., & Neugebauer, G. 1978, AJ, 83, 1240
Paresce, F. 1992, Hubble Space Telescope Faint Object Camera Instrument Handbook (St Sci)
Percival, J. W. 1992, High Speed Photometer Pulse Timing and Light Curve Reduction (Space Astronomy Laboratory, University of Wisconsin)
Percival, J. W. 1993, PASP, 105, 551
Percival, J. W., *et al.* 1993, ApJ, 407, 276
Press, W. H., Flannery, B. P., Teukolsky, S. A., & Vetterling, W. T. 1988, Numerical Recipes in C (Cambridge University Press, Cambridge)

Rosen, P. A., Tyler, G. L., & Marouf, E. A. 1991a, Icarus, 93, 3
Rosen, P. A., Tyler, G. L., Marouf, E. A., & Lissauer, J. J. 1991b, Icarus, 93, 25
Seidelmann, P. K., Ed. 1992, Explanatory Supplement to the Astronomical Almanac (University Science Books, Mill Valley, CA)
Showalter, M. R. 1991, Nature 351, 709
Slivan, S. 1991, A Preliminary "Spot-Check" of HST Orbit Information (MIT, Cambridge)
Smart, W. M. 1977, Textbook on Spherical Astronomy, 6th ed. (Cambridge University Press, Cambridge)
Standish, E. M. 1990, A&A, 233, 252
Standish, E. M., Newhall, X. X., Williams, J. G., & Yeomans, D. K. 1992, in Explanatory Supplement to the Astronomical Almanac, edited by P. K. Seidelmann (University Science Books, Mill Valley, CA), p. 279
Sybert, C. B., Bosh, A. S., Sauter, L. M., Elliot, J. L., & Wasserman, L. H. 1992, AJ, 103, 1395
USNO 1992, The Astronomical Almanac for the Year 1992 (U.S. Government Printing Office, Washington)
Wolfram, S. 1991, Mathematica. 2nd ed. (Addison-Wesley, Redwood City, CA)

1993AJ....106.2544E

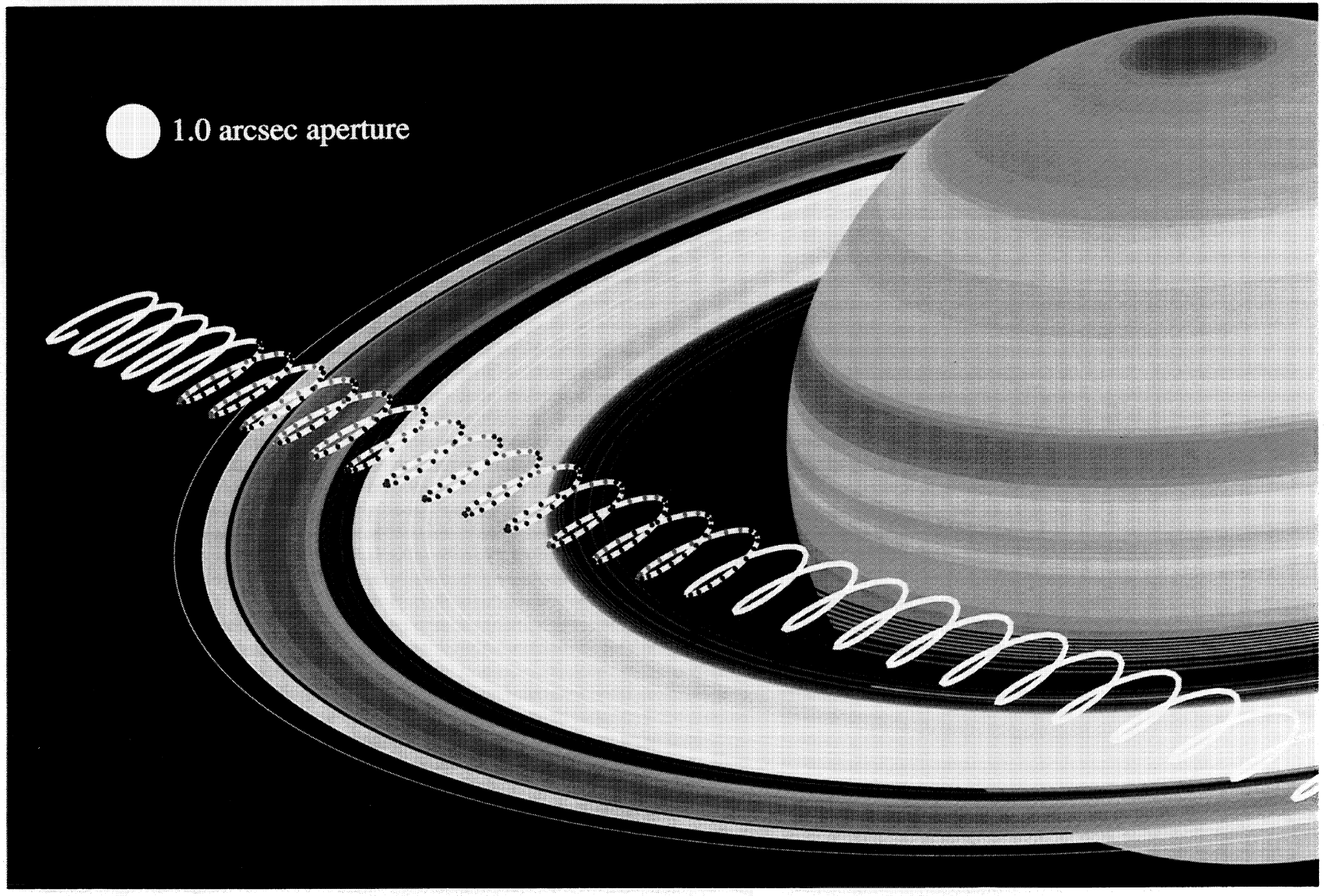

Fig. 4. The path of the star GSC 6323-01396 relative to Saturn's rings during the 1991 October 2–3 occultation, as distorted by spacecraft parallax. Dots are shown at 5 min intervals for the 20 h period of our observations. The spacecraft's motion around the Earth takes it behind our planet (as seen from Saturn) for almost half of each orbit; these Earth occultations are shown in blue. Red dots indicate SAA passages, also unobserved. The remaining stretches of the looping occultation track, shown in green, represent the windows of observability during which data were taken by the HSP's PMT and VIS detectors in "star-sky" mode.

Elliot *et al.* (see page 2551)